

**Warsaw University
Faculty of Physics**

Mateusz Kapusta

Index number: 431289

Search for dormant black holes in the OGLE data.

Bachelor degree in the field of Astronomy

Thesis written under supervision of
dr Przemysław Mróz
Astronomical Observatory
Warsaw University

Warsaw, May 2023

Abstract

In the work analysis of light curves from OGLE data was performed with the goal to look for objects with possible black hole companions based on the ellipsoidal modulation of light curves. Each object is examined using the spectral energy distribution fit, allowing one to distinguish between stars composed of two objects with different temperatures and single objects. The selection process resulted in fourteen potential objects out of which one turned out to be the spotted star, while the rest are considered black hole binaries candidates. Detailed analysis of objects is conducted estimating basic physical parameters such as temperature, mass, radius, and, in some cases, estimate of radial velocity. Although in the end an alternative explanation for ellipsoidal modulation is given, no conclusion is reached as objects should be further observed spectroscopically to accept or reject the hypothesis about compact companions.

Keywords

Compact Objects, Ellipsoidal variables

Thesis title in Polish language

Poszukiwanie uśpionych czarnych dziur w danych z przeglądu OGLE.

Contents

1. Introduction	3
2. Theoretical considerations	6
2.1. Morris & Naftilan expression	6
2.2. Amplitude correction	7
2.3. Limitations	7
2.4. Modified mass ratio	8
2.5. Selection process	8
3. Observational data	10
3.1. Description of data and preprocessing	10
3.2. Spectral Energy Distribution	13
4. Results	18
4.1. Physical parameters of objects	18
4.2. Radial velocity semiamplitude estimation from Gaia DR3 data	19
4.3. Detailed analysis of objects	20
4.3.1. GD1070.18.22288	20
4.3.2. SMC720.28.40576	24
4.3.3. Remaining objects	27
5. Discussion & Conclusions	30
Bibliography	31
Appendices	35
A. Light curve & SED plots	37
B. Semiamplitude estimate from Gaia DR3	51
C. Light curve modelling	52

Chapter 1

Introduction

According to the current knowledge, O type stars (which are more massive than $20 M_{\odot}$) end their evolution as black holes, further investigation suggests the existence of $\mathcal{O}(10^8)$ stellar mass BHs (Brown & Bethe, 1994) in our Galaxy. Despite a huge theoretical expectation, only a few tens of such objects have been found up to day. Since the discovery of the first black hole binary Cygnus X-1 many researchers have tried to tackle the problem employing numerous methods with particular success achieved in the field of X-ray based observations. Although such observations can be a great tool for black hole search, there are quite limited, as formation of such systems is rare (Zwart et al., 1997). Since the beginning of LIGO/VIRGO observations of merging black holes, interest in the progenitors of black hole merger events began to grow. Despite many surveys and theoretical works, no conclusions were reached about formation mechanisms for many black hole mergers.

The vast majority of black hole binaries were discovered due to X-ray emission from an accretion disc that is forming in a system. X-ray emitting objects can be roughly grouped into two categories: low-mass X-ray binaries and high-mass X-ray binaries (referred to as LMXB and HMXB). Low-mass binaries are composed of a compact object that is accreting matter from a low-mass companion overflowing its Roche lobe. On the other hand, high-mass X-ray binaries accrete matter from a stellar wind created by a high-mass companion star. The X-ray emission from the X-ray binaries is mostly transient in character (Belloni & Motta, 2016) due to the instability of the accretion disc (Lasota, 2001). Many of the X-ray binaries can remain undetected in the low-accreting regime for long periods, hence an all-sky monitoring in X-rays is necessary. According to Corral-Santana et al. (2016) only 64 stellar BH X-ray binaries have been detected to the present day, while only 5 of them are considered persistent sources. Of all those sources, only around ~ 20 of them are dynamically confirmed (from dynamically confirmed binaries only Cygnus X-1 is persistent). The rest of the candidates were not observed spectroscopically, as they are faint in quiescence, distant, or lie in high-extinction regions. Although most of the observed BH binaries emit X-rays such systems should be outnumbered by nonaccreting binaries (Langer et al., 2020). The estimated total number of X-ray black holes in the Milky Way is around $\sim 10^3$ (Corral-Santana et al., 2016), suggesting that only small fraction of such systems was discovered. It is hard to determine how many of those binaries can be detected as search for such transient objects can be problematic. Nevertheless, both theoretical and observational arguments agree that that potential population of black hole X-ray binaries is rather limited.

In recent years new stellar mass BH candidates have been found due to the new methods not based on X-ray emission. New generations of sky surveys including spectroscopic surveys like APOGEE, LAMOST and GALAH can provide radial velocity information for millions

of stars. Such information itself can be used to search for compact objects and there are numerous candidates for compact binaries that are dormant in the X-ray including black hole binaries (Liu et al. (2019), Jayasinghe et al. (2019), Shenar et al. (2022), Lennon et al. (2022), Thompson et al. (2019)). Although many of those claims have been disputed, one can expect such surveys to provide an increasing number of potential black hole binaries. Unfortunately, even wide-field multi-fibre spectroscopic devices cannot observe as many objects at once as wide-field photometric devices, limiting the size of the sample that can be studied with this type of survey. There are also new discoveries of potential black hole binaries using Gaia astrometric observations coupled with spectroscopic follow-up observations (El-Badry et al., 2022, 2023). Binaries with sufficiently long periods paired with low parallaxes allow one to resolve components of binary and trace apparent movement on the sky. This type of observation is available only for a relatively small sample of objects (~ 30000) at the moment, but with the next releases of Gaia data, this number is expected to increase significantly. Astrometric observations are powerful and on their own enable one to estimate masses of objects via the astrometric mass function. Compared to X-ray observations, astrometric measurements allow one to estimate parameters of objects with much better accuracy, as they allow one to infer an inclination of a binary. This crucial parameter is very hard to constrain in most of systems, in X-ray binaries it is usually estimated by modelling the ellipsoidal effect visible in the light curve, which can lead to mass overestimation as demonstrated by (Kreidberg et al., 2012).

The third kind of observation that allows one to search for black holes, which already led to the discovery of an isolated stellar black hole (Sahu et al., 2022), is microlensing. As the massive object passes in front of a source, magnified images of the source object are created; the total observed luminosity of such an object will increase. Unfortunately photometric observations on their own do not allow one to estimate the mass of the lens. To infer parameters of objects taking part in the event, one needs to resolve images of the source and trace its relative position during the event. There is a possibility that some of the microlensing events already observed by Gaia will leave a visible signal in the astrometric data that will be released as part of DR4 (as, for example, in the case of Kruszyńska et al. (2022)). Microlensing is the only viable method that can be used to detect isolated black holes, as such objects are not expected to emit X-rays from the interstellar medium accretion. As there is little information about such systems it is hard to specify what can be potentially observed although some estimations (Sajadian & Sahu, 2023) suggest that next generation microlensing surveys as the Roman Telescope should observe astrometric signals from few tens of isolated black hole microlensing events.

Recent advances in technology allowed one to open a new observational window as in 2016 LIGO/VIRGO gravitational wave observatories announced discovery of the first black hole - black hole merger. This was soon followed by more discoveries including black hole mergers as well as neutron star mergers. Since the beginning of the programme many interesting objects have been observed that challenge current knowledge about the black hole formation. Up to date it was believed that there are two forbidden regions in the black hole mass distribution: a low-mass gap and a high-mass gap. Although the high-mass gap is the result of the so-called pair instability, there is no consensus on the low-mass gap. In the core of most massive stars, temperature can reach critical value above which radiated photons can be easily converted into electron/positron pair. Such a reaction can lead to a decrease in the pressure, resulting in implosion of the stellar core. Detailed analysis suggests that due to pair instability no black holes with masses in the range ($50M_{\odot}$, $130M_{\odot}$) should exist. The lower mass gap, on the other hand, was proposed, as to date no X-ray binaries with masses of compact objects in the range ($3M_{\odot}$, $5M_{\odot}$) have been discovered. It was contested whether it is only a

selection effect or whether there are really no black holes in this range. Although there were some theoretical arguments for the low mass gap (Belczynski et al., 2012) gravitational wave astronomy challenged those claims as merging objects from low-mass gap and high-mass gap have been observed. Although it is possible that those black holes formed via merging of smaller objects, the origin of those mergers puzzles the community up to this day. Due to the aforementioned discrepancies, detection of black hole binaries would allow one to get a better insight into evolutionary channels of gravitational wave progenitors.

Both X-ray surveys and astrometric solutions have some limitations as each of them allows only one end of the binary widness spectrum to be probed. In recent years, a new approach was proposed with the aim of finding objects that almost fill Roche lobes. One can expect that the light curve of such an object is dominated by ellipsoidal modulation caused by the tidal distortion of the primary star. This approach has great advantage because the photometric data are very vast in contrast to the spectroscopic one. The relative potential of this approach was shown by Masuda & Hotokezaka (2019), it is estimated that a light curve modulation due to the ellipsoidal effect can be enough to track down at least a few of them in the TESS data. Other notable cases include the series of publications Gomel et al. (2021a,b,c) on which this work is based. Publications presented a new way to search for this type of objects using the publicly available list of ellipsoidal variables in the direction of the Galactic Bulge from the OGLE database (Soszyński et al., 2016). This approach itself provides a rather good and robust way to look for systems with high mass ratios. In chapter 2 a theoretical introduction to ellipsoidal modulation will be given, and in the following chapters a method is employed to search for candidates for BH in the OGLE database.

Chapter 2

Theoretical considerations

2.1. Morris & Naftilan expression

Let us consider a binary system with a semi-major axis of orbit a , a primary star mass M_1 , and a radius R_1 which is tidally disrupted by a second object with a mass M_2 . One can define the mass ratio $q = \frac{M_2}{M_1}$ and want it to be as high as possible, which indicates that the primary star is less massive than the (hopefully invisible) companion. Until today many publications have tackled the problem of ellipsoidal modulation, including Kopal (1959) leading to formula proposed by Morris & Naftilan (1993)

$$\begin{aligned} \frac{\Delta L}{L} &= \frac{\alpha_1}{\bar{L}/L_0} \left(\frac{R_1}{a} \right)^4 q (4 \sin i - 5 \sin^3 i) \cos \varphi \\ &\quad - \frac{1}{\bar{L}/L_0} \left(\alpha_2 \left(\frac{R_1}{a} \right)^3 q \sin^2 i + \beta_2 \left(\frac{R_1}{a} \right)^5 q (6 \sin^2 i - 7 \sin^4 i) \right) \cos 2\varphi \\ &\quad - \frac{5}{3} \frac{\alpha_1}{\bar{L}/L_0} \left(\frac{R_1}{a} \right)^4 q \cos 3\varphi \end{aligned} \quad (2.1)$$

$$\frac{\Delta L}{\bar{L}} = A_1 \cos \varphi + A_2 \cos 2\varphi + A_3 \cos 3\varphi$$

where φ denotes the relative phase, i the orbital inclination, L_0 is the luminosity *without tidal disruption*, while \bar{L} stands for the mean luminosity of the primary star. From this point onwards, equation 2.1 will be referred to as MN93. The coefficients α_1 , α_2 and β_2 are connected to the limb darkening coefficient u and the gravity darkening coefficient τ via equations

$$\alpha_1 = \frac{15u(2 + \tau)}{32(3 - u)}, \quad (2.2)$$

$$\alpha_2 = \frac{3(15 + u)(1 + \tau)}{20(3 - u)}, \quad (2.3)$$

$$\beta_2 = \frac{15(1 - u)(3 + \tau)}{64(3 - u)}. \quad (2.4)$$

Both values \bar{L} and L_0 are also related and can be found through the following equation

$$\bar{L} = L_0 \left(1 + \frac{1}{9} \left(\frac{R_1}{a} \right)^3 (2 + 5q)(2 - 3 \sin^2 i) \right). \quad (2.5)$$

Formulas can be rewritten in a more suitable form after the substitution

$$\frac{R_1}{a} = \frac{R_1}{R_{\text{Roche}}} \frac{R_{\text{Roche}}}{a} = E(q) f \quad (2.6)$$

where R_{Roche} denotes a radius of the Roche lobe, f stands for a Roche lobe fillout and $E(q)$ denotes a ratio of the Roche lobe radius to the semi major axis which can be described by the classic Eggleton formula (Eggleton, 1983)

$$E(q) = \frac{0.49q^{-\frac{2}{3}}}{0.6q^{-\frac{2}{3}} + \log(1 + q^{-\frac{1}{3}})}. \quad (2.7)$$

MN93 equation in its original form is valid only for small values of f and q , making it unsuitable for any kind of search, as one would like to find objects with high values of q . Following Gomel et al. (2021a), the expression for a second harmonic coefficient is assumed to be dominated by the first term, resulting in the final formula

$$A_2 \approx \frac{1}{L/L_0} \alpha_2 E(q)^3 f^3 q \sin^2 i. \quad (2.8)$$

2.2. Amplitude correction

There are few approaches that one can take to extend the MN93 formula, in this work the original formulation from Gomel et al. (2021a) was adopted. In the original work, each coefficient was multiplied by a correction $C_i(q, f, i)$ calculated using the PHOEBE simulation software. For each Fourier coefficient, a relevant model was fitted to PHOEBE data and then compared, allowing one to find such function $C(q, f, i)$ that

$$\left(C(q, f, i) - \frac{A_{\text{Phoebe}}}{A_{\text{MN93}}} \right)^2 \quad (2.9)$$

is minimised. In Gomel et al. (2021a), the following functions were chosen for the second and third correction coefficients

$$C_2(q, f, i) = 1 + \left(0.0379 + \frac{0.005}{0.0446 + q} \right) \left(\frac{f}{1.0909 - f} \right) \quad (2.10)$$

$$C_3(q, f, i) = 1 + \frac{(1 + 0.0698q \sin^2 i)f^6 + 0.2075 \cdot f^2}{(2.0223 + 0.3880 \ln q)f + \sin^4 i} \quad (2.11)$$

as they have a closed analytical form and a small relative error.

2.3. Limitations

In the previous section, a new corrected formula was introduced allowing one to predict Fourier series coefficients based on physical parameters q, f, i . In reality, a light curve can be influenced by more than one modulation, limiting usability of the presented formula. To begin with, the MN93 formula is valid only for circular orbits. To remove that limitation, one can reproduce the results using other types of expansion such as Engel et al. (2020). Moreover in the case of compact binary there may be need to take into account the relativistic beaming effect. Following Loeb & Gaudi (2003)

$$F_\lambda = F_{\lambda,0} \left(1 - B \frac{v_r}{c} \right) \quad (2.12)$$

where F_λ is the spectral energy density, v_r is the radial velocity, and B is the coefficient defined as $B = 5 + \frac{\partial \ln F_\lambda}{\partial \ln \lambda}$. One needs to emphasise that the relativistic beaming effect does not affect the second or the third harmonic coefficient. This is purely due to the fact that beaming is caused by motion, while the main tidal effect is in the second harmonic and can be interpreted as an effect connected purely to the position. This important fact makes the second harmonic best for any search when the goal is to predict physical parameters based on the amplitude of harmonics. There are also a few other effects that one can consider such as the reflection effect, detailed analysis can be found in Gomel et al. (2021a).

2.4. Modified mass ratio

After deriving the expression for the second harmonic coefficient, one can introduce the *modified mass ratio* following Gomel et al. (2021b). As can be verified, $A_2(q, f, i, \alpha)$ is an increasing function of both $\sin i$ and f . This allows to introduce q_{mmr} such that

$$A_2(q_{mmr}, 0.98, \pi/2, 1.2) = \tilde{A}_2 \quad (2.13)$$

where \tilde{A}_2 is the measured value of the second harmonic amplitude. Here, $f = 0.98$ is assumed as in the original approach, since the aim is to detect barely overflowing primary components. These definitions ensure that q_{mmr} is the lower bound of the true mass ratio for any values of i and $f < 0.98$. This property is crucial and provides a simple way to search for objects with potentially compact companions. The most important parameter on which the whole analysis is based is α_2 . Following the original work $\alpha_2 = 1.2$ was set for observations in the I band and standard deviation $\Delta\alpha_2 = 0.1$ was also assumed. This value solely represents the effects of temperature, gravity, and chemical composition, which is very important, as it encapsulates all unknown parameters. The exact value of the parameter greatly influences the modified mass ratio, which makes inference of the mass impossible without precise knowledge of α_2 . The detailed dependence of α_2 on the effective temperature in the case of $\log g = 4$ and $[Fe/H] = -1$ based on the limb and gravity darkening coefficients produced by Claret (2000) is presented in the figure 2.1. This fact led the authors of the method to introduce the second parameter, which was originally defined as the 16th percentile of the estimator q_{mmr} . The sole role of this parameter is to take into account the uncertainty of α acting as the lower bound of q_{mmr} . In this work, another parameter was introduced denoted as \tilde{q}_{mmr} and defined using the equation

$$A_2(\tilde{q}_{mmr}, 0.98, \pi/2, 1.1) = \tilde{A}_2 - \Delta A_2$$

where ΔA_2 is the uncertainty associated with the estimate of the A_2 coefficient. This approach not only allows one to filter out those stars that can have large amplitude due to the surprisingly high value of α_2 , which is taken into account by decreasing α_2 in the definition 2.4 to 1.1, but also those with a high amplitude and a relatively high uncertainty ΔA_2 .

2.5. Selection process

In order to provide a reliable and robust way to search for compact companions, the following procedure was used. For each object, two coefficients q_{mmr} and \tilde{q}_{mmr} were calculated, and each object for which $\tilde{q}_{mmr} > 1$ was qualified as a candidate for a star with a compact companion. Second, each object with amplitude $\tilde{A}_2 > 0.24$ was removed from the list. One can find using 2.13, that a mass ratio of order $q_{mmr} \approx 1000$ is needed to obtain a configuration with such a great amplitude suggesting that modulation is not due to the ellipsoidal effect,

but rather caused by other type of star variability. The exact threshold of \tilde{A}_2 can be a matter of debate due to the dependence on α_2 which is unknown.

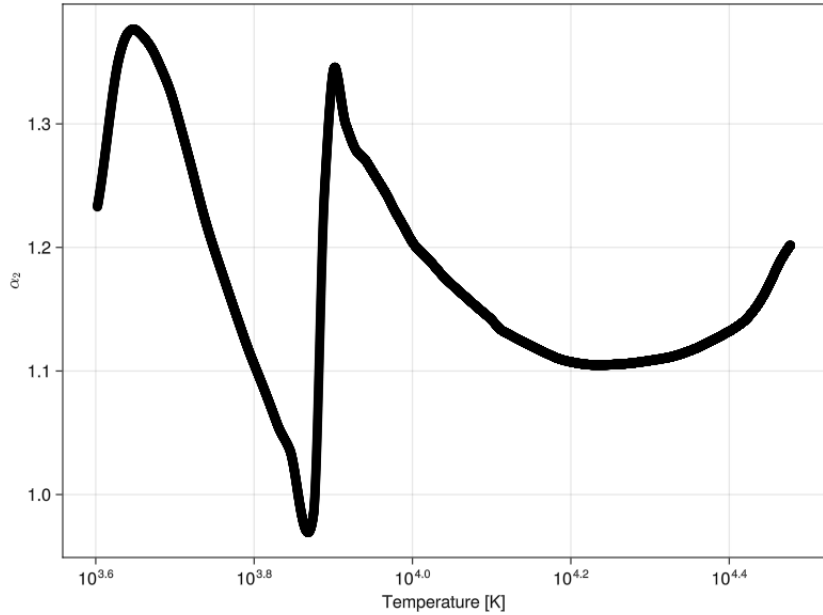


Figure 2.1: Dependence of the parameter α_2 for the I band vs. the effective temperature for stars with $\log g = 4$ and $[Fe/H] = -1$.

Chapter 3

Observational data

3.1. Description of data and preprocessing

From the OGLE (Udalski et al., 1992) database following two samples were analysed using aforementioned method:

- objects from the direction toward Magellanic Clouds. The sample consist of ellipsoidal stars from Pawlak et al. (2016) with objects supplemented by Przemysław Mróz,
- ellipsoidal variabales from the direction toward the Galactic Bulge and the Galactic Disc cross-matched by Przemysław Mróz with the Gaia DR3 (Collaboration et al., 2022). Sources with $rv_amplitude_robust > 100$ km/s were selected.

The light curves used in the analysis were collected during the 4 th season of OGLE Udalski et al. (2015), and were collected in the I band. Detailed positions of objects from the original samples in the sky are presented in the figure 3.1. Then for each entry the nearest Gaia source was found and for objects without statistically significant parallax (value higher than three times it's statistical deviation) a color-magnitude diagram using the Gaia data was constructed and is presented in the figure 3.2 (with division between SMC and LMC/MBR). Similarly a color-magnitude diagram was constructed for objects with statistical significant parallax and presented in the figure 3.3. Most of the objects in the samples have a relatively short period (< 3 d); a detailed period distribution is presented in the figure 3.4.

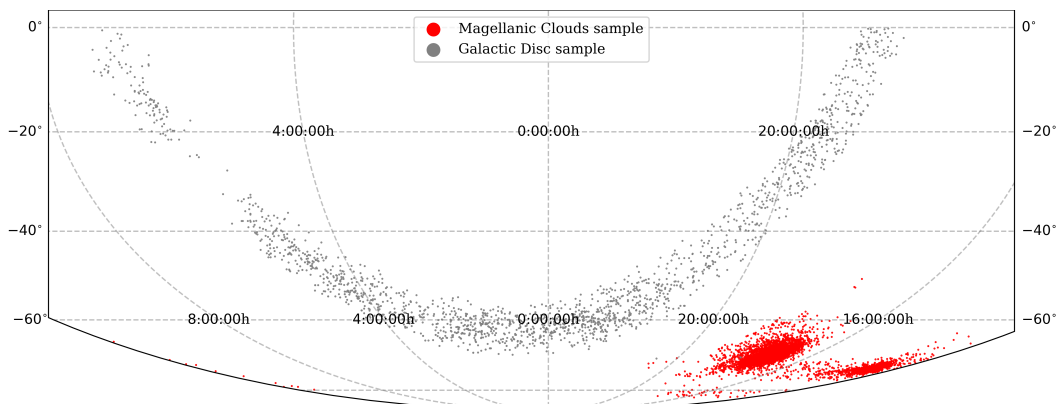


Figure 3.1: Positions of objects from the samples across the southern sky.

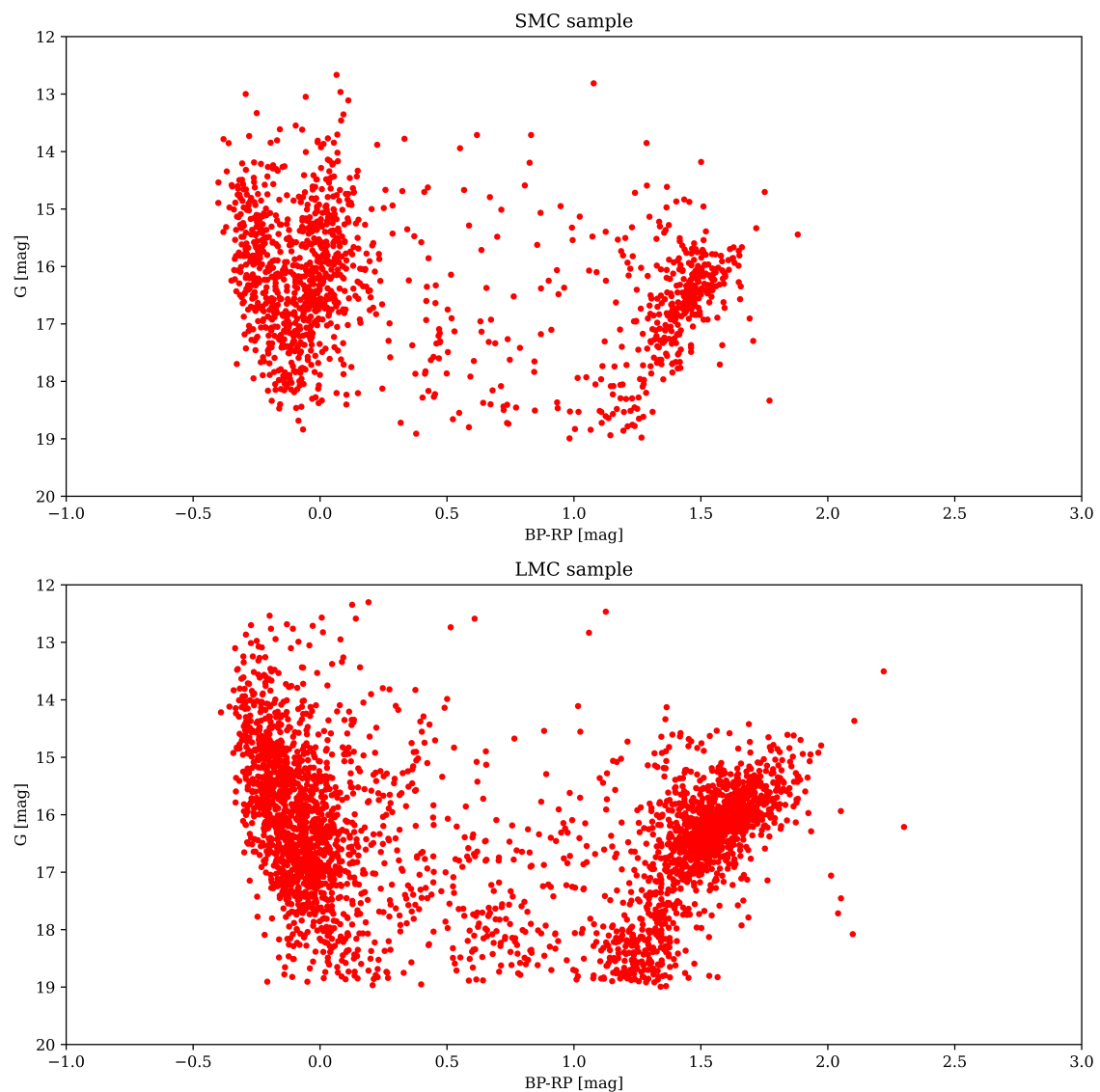


Figure 3.2: A color-magnitude diagram of Gaia counterparts potentially residing in Magellanic Clouds (without statistically significant parallax).

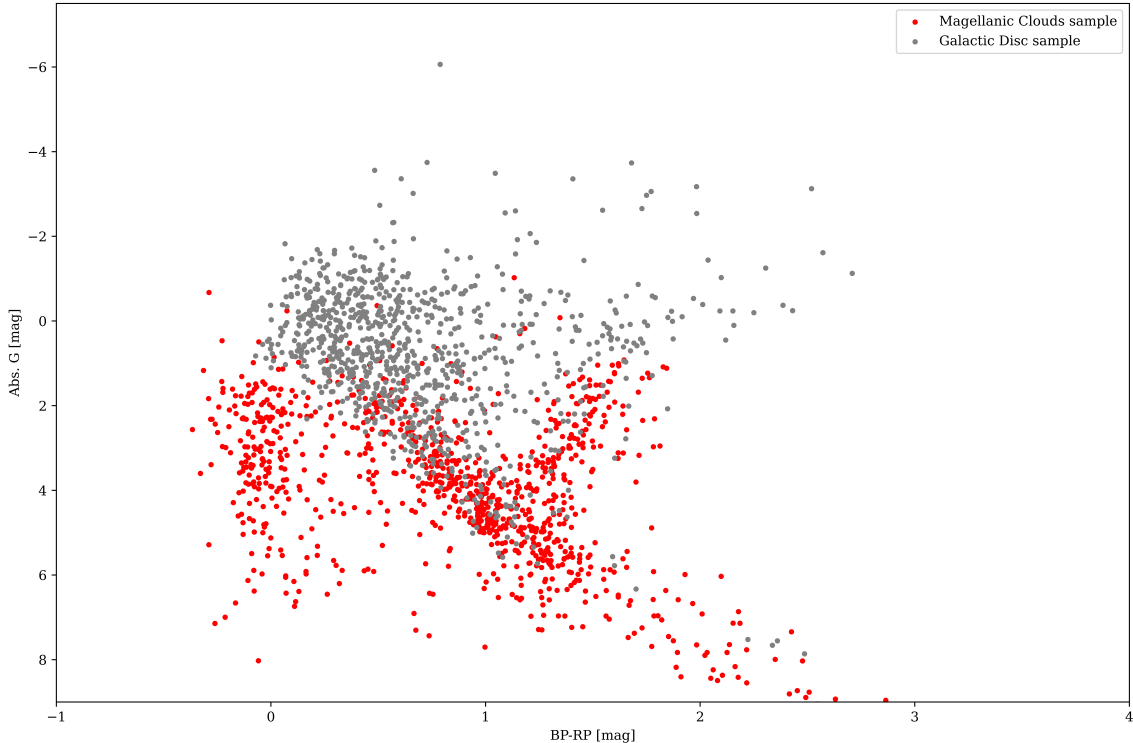


Figure 3.3: A color-magnitude diagram of Gaia counterparts with statistically significant parallax.

As a first step of preprocessing objects with brightness lower than 17 mag were removed as faint stars wouldn't be suitable for a radial velocity determination with the usage of high resolution spectroscopy. Each object was analysed using the ANOVA (analysis of variance) method (Schwarzenberg-Czerny, 1989) to determine the period. Then each light curve was fitted with the 4th degree harmonic model

$$I(t) = A_0 + \sum_{i=1}^4 \left[A_{1i} \sin \left(2\pi i \frac{t}{P} \right) + A_{2i} \cos \left(2\pi i \frac{t}{P} \right) \right] \quad (3.1)$$

with the sigma clipping threshold set at 3σ allowing to determine amplitudes of coefficients from the relationship $A_i = \sqrt{A_{1i}^2 + A_{2i}^2}$. This least-squares problem was solved using the Levenberg-Marquardt algorithm with an error estimate based on a covariance matrix. Subsequently, the minimum mass ratio q_{mmr} and its lower bound \tilde{q}_{mmr} were calculated and the previously described procedure of selecting candidates was carried out. Objects with light curves indicating other type of variability than ellipsoidal one were removed together with those with periods longer than 50 d. According to the main assumption in the analysis objects should be composed of stars nearly filling their Roche lobe, so a rather short period is suggested. The exact value of the threshold can be debated; here it is used as a mean to remove pulsating stars that pollute the sample. After this part of the preprocessing, only 41 objects from the first sample were left together with 22 objects from the second sample.

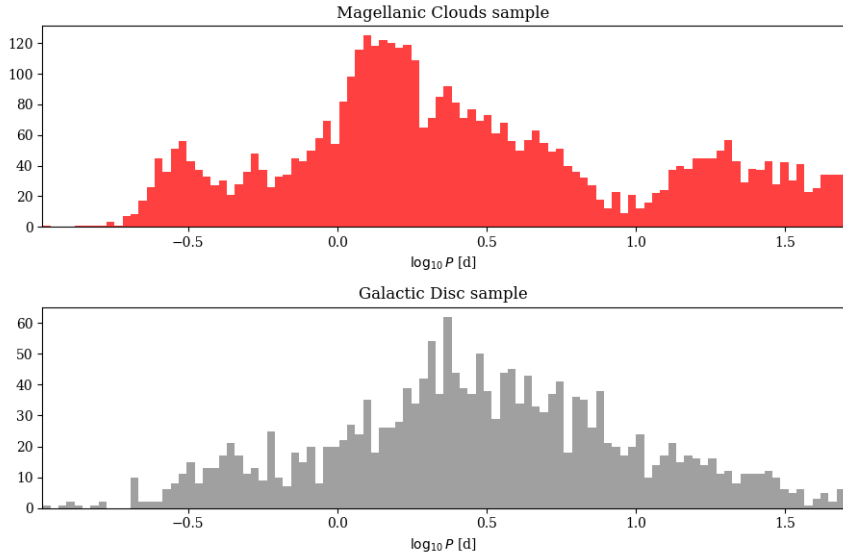


Figure 3.4: Distribution of periods from the analysed samples.

3.2. Spectral Energy Distribution

Each object was cross-matched with the Gaia DR3 catalogue to obtain parallax (hereinafter denoted as π_0 together with its uncertainty denoted as σ_π) estimates of the objects. If the parallax was statistically significant ($\pi > 3\sigma_\pi$) it was used to derive the distance to the object. For objects towards Magellanic Clouds many entries lacked a statistically significant parallax, indicating that they really reside in Magellanic Clouds and do not line up accidentally. In this case, the distance estimate d_0 and the distance uncertainty σ_d were based on Jacyszyn-Dobrzeniecka et al. (2016). It is assumed that the presented distribution of Cepheids reflects the underlying distribution of stars in the sample. In the case of LMC and SMC the assumed distance estimates were $d_{LMC} = 49.93 \pm 1.79$ kpc and $d_{SMC} = 64.62 \pm 4.95$ kpc, respectively.

To further investigate the nature of objects, a spectral energy distribution analysis was performed with two models: a single star model and a double star model. Main goal of this type of analysis is to use a photometry from various bounds to reconstruct a whole spectral characteristic and hence infer parameters (like a temperature and a luminosity) of an object. The single star model depends on three free parameters: a logarithm of temperature $\log_{10} T$ (expressed in kelvins), a logarithm of luminosity $\log_{10} L$ (expressed in L_\odot) and the third parameter was either a parallax (if one was measured), or a distance if it wasn't available. In the case of the double-star model, there were two additional parameters describing the second star $\log_{10} T_2$ and $\log_{10} L_2$. In the case of the first model star, it was assumed to be a main sequence object (MS) with $\log g = 4$. In the double star model the primary star was assumed to have $\log g_1 = 4$ as in the first case, while the second object was assumed to be a giant with $\log g_2 = 2$. Objects with a statistically significant parallax were assumed to have solar-like metallicity ($Z = 0.013$) as they reside inside the Galactic disc. Objects in Magellanic Clouds were assumed to have a metallicity equal to $Z = 0.010$ in the case of LMC/MBR and $Z = 0.005$ in the case of SMC. The BaSeL library of stellar spectra (Lejeune et al., 1998) was used to find the spectrum for any given $\log_{10} T$, $\log_{10} L$, d by means of the

interpolation as implemented in the Python library `pystellib`¹. Then the theoretically calculated stellar spectrum is then processed using the `pyphot`² Python library, yielding a magnitude in a required filter.

In order to find a set of best-fitting parameters, a Bayesian approach was adopted. Let's denote a set of observed magnitudes as \tilde{m}_i , theoretically predicted magnitudes as m_i while errors of magnitudes as σ_i . Let's denote by $\mathcal{U}(a, b)$ a uniform distribution with the support in the form of an interval $[a, b]$ and $\mathcal{N}(\mu, \sigma^2)$ as a normal distribution with a mean μ and a variance σ^2 . In order to prepare the Bayesian model one need to specify a probability distribution that will allow to evaluate a likelihood of data. Each of the observed magnitudes \tilde{m}_i is expected to be normally distributed with a mean m_i and a variance σ_i^2 , while the prior distributions for each of the three parameters are uniform in the case of $\log_{10} T$ and $\log_{10} L$, or normal in the case of a distance or parallax. A detailed model can be written as:

$$\begin{aligned} \log_{10} T &\sim \mathcal{U}(3.31, 4.6) \\ \log_{10} L &\sim \mathcal{U}(-3, 5) \\ d &\sim \mathcal{N}(d_0, \sigma_d^2) \text{ or} \\ \pi &\sim \mathcal{N}(\pi, \sigma_\pi^2) \\ \tilde{m}_i &\sim \mathcal{N}(m_i(\log_{10} T, \log_{10} L, d), \sigma_i^2) \text{ or} \\ \tilde{m}_i &\sim \mathcal{N}(m_i(\log_{10} T, \log_{10} L, \pi), \sigma_i^2) \end{aligned} \tag{3.2}$$

where $m_i(\log_{10} T, \log_{10} L, d)$ is written to indicate that a predicted magnitude is a function of parameters. Similarly, one can write down the second model together with priors for the parameters

$$\begin{aligned} \log_{10} T_1 &\sim \mathcal{U}(3.31, 4.6) \\ \log_{10} L_1 &\sim \mathcal{U}(-3, 5) \\ \log_{10} T_2 &\sim \mathcal{U}(3.444, 4.21) \\ \log_{10} L_2 &\sim \mathcal{U}(-3, 5) \\ d &\sim \mathcal{N}(d_0, \sigma_d^2) \text{ or} \\ \pi &\sim \mathcal{N}(\pi, \sigma_\pi^2) \\ \tilde{m}_i &\sim \mathcal{N}(m_i, \sigma_i^2) \end{aligned} \tag{3.3}$$

where explicit dependence of m_i on the parameters was hidden for clarity. In both cases, the normal distribution is truncated to positive numbers, as negative parallax/distance solutions are not permitted. The range of a logarithm of temperature is limited due to the boundaries of the library, whereas a logarithm of luminosity is set in the boundaries to eliminate nonphysical solutions. Under those assumptions, a log-likelihood function can be written as

$$\begin{aligned} \ln \mathcal{L} &= - \sum_i \frac{(\tilde{m}_i - m_i)^2}{2\sigma_i^2} - \frac{(d - d_0)^2}{2\sigma_d^2} \text{ or} \\ \ln \mathcal{L} &= - \sum_i \frac{(\tilde{m}_i - m_i)^2}{2\sigma_i^2} - \frac{(\pi - \pi_0)^2}{2\sigma_\pi^2} \end{aligned} \tag{3.4}$$

depending whether a distance or a parallax was used.

Following catalogues were used to assemble SEDs:

¹<https://github.com/mfouesneau/pystellib>

²<https://github.com/mfouesneau/pyphot>

1. Catalogues shared by both samples of objects:
 - 2MASS survey (Skrutskie et al., 2006),
 - Gaia DR2 (Gaia Collaboration et al., 2018),
 - VISTA Hemisphere Survey DR5 (McMahon et al., 2021),
 - ALLWISE/WISE survey (Wright et al., (2010), Cutri et al., (2021)),
 - GALEX Survey (Bianchi et al., 2011),
 - Denis survey (Denis, 2005),
 - SkyMapper DR1/DR2 (Wolf et al., (2018), Onken et al., (2019)),
 - XMM Optical Monitor serendipitous sources catalog (Page et al., 2012).
2. Catalogues exclusive to the Magellanic Clouds sample:
 - VISTA Magellanic Cloud survey DR4 (Cioni et al., 2017),
 - Spitzer SAGE survey: SMC and LMC (Meixner et al., (2006), Gordon et al., (2011)),
 - Denis catalogue of objects in Magellanic Clouds (Cioni et al., 2000),
 - Magellanic Clouds Photometric Survey: SMC and LMC (Zaritsky et al., 2002, 2004).
3. Catalogues exclusive to the Galactic Disc sample:
 - Bochum Galactic Disc survey (Hackstein et al., 2015),
 - AAVSO Photometric All Sky Survey DR9 (Henden et al., 2015),
 - VISTA Variables in Via Lactea Survey DR2 (Minniti et al., 2017),
 - GLIMPSE source catalog (Spitzer Science, 2009).

In the case of Magellanic Clouds, extinction estimates were based on the map Skowron et al. (2021), while in the case of Galactic disc extinction it was obtained using the Python library `mwdust` (Bovy et al., 2016) with the 3D dust map being a combination of Green et al. (2019), Greiner et al. (2001), Drimmel et al. (2003). As the OGLE does not cover positions of all objects, those without an estimated extinction were assumed to be zero. In the calculations, the Cardelli extinction law (Cardelli et al., 1989) with $R_V = 3.1$ was assumed and the Python implementation from `extinction`³ was used. Using the described setup, the MCMC Python-based library `emcee`⁴ (Foreman-Mackey et al., 2013) was used to construct the set⁵ of routines used to sample from the posterior of the models, providing estimates of parameters together with associated uncertainties. Other packages used in the study are `astroquery` (Ginsburg et al., 2019), `corner` (Foreman-Mackey, 2016) and `astropy` (Astropy Collaboration et al., 2022). Each sampling was carried out with 32 walkers for 2000 steps (with 750 burn in); in the case of a double model, each sampling was followed by a second one with starting conditions sampled from the first chain. A chain convergence was checked with a corner plot, two example plots are presented in the figure 3.5. In order to help to decide between models the BIC score was used

$$BIC = k \log n - 2 \ln \mathcal{L} \quad (3.5)$$

³<https://extinction.readthedocs.io/en/latest/index.html>

⁴<https://emcee.readthedocs.io/en/stable/>

⁵<https://github.com/Wesenheit/Iris>

where k is a number of estimated parameters and n is a number of data points. From all objects thirteen were selected based on the fit with the single star model. If the BIC score was lower in the case of the single star model star was selected as a candidate. If the BIC score was lower in the case of the double star model object was rejected unless

- the most luminous star in the double star model is significantly brighter than other and has $\log g = 2$,
- some stars in the model have unphysical solutions (i.e. luminosity of the star is too low for star with $T = 20000$ K).

There might be a possibility that the photometry can be better fitted with lower gravity and hence, despite the fact that binary is single in nature, it will always be fitted better with a double star model (because in a single star model $\log g = 4$). There can be also a possibility that a star with slight excess in UV will be better fitted in the double star model than in single star model because the metallicity in the single star model is slightly wrong. This is sometimes visible in the SED fit, as the double star model in such case outputs a very hot companion with a very low radius $R \approx 0.1 R_{\odot}$. All of those factors are taken into account and each object was manually inspected in order to check if it qualifies as a single star.

One of the objects was selected due to the observed X-ray emission that can indicate the existence of the accretion disc. The key parameters of the objects are listed in the table 3.1. The parallax solution for LMC751.15.2886, initially considered statistically insignificant, was adopted because the ratio of parallax to statistical deviation was rather high (2.975) and the Ruwe parameter (renormalised unit weight error) was close to unity (1.064). After this change, only one object from the selected sample is considered not to reside in the Galaxy.

Name	Period [d]	q_{nmr}	\tilde{q}_{mmr}	Ra [deg]	Dec [deg]	A_0	A_1	A_2	A_3	A_4	π_0 [mas]
BLG986.08.7	0.5132	1.46	1.03	260.451241	-43.019464	12.192	0.0028	0.0985	0.0039	0.0093	1.199
GD2246.03.18414	0.4270	2.29	1.55	179.327372	-57.091968	12.0764	0.0045	0.1090	0.0030	0.0106	1.410
GD1097.20.23000	0.4570	9.73	5.18	252.108419	-44.137004	11.782	0.0008	0.1414	0.0029	0.0200	1.775
GD1448.27.17	1.2410	1.77	1.23	139.969949	-45.759178	11.875	0.0115	0.1035	0.0030	0.0056	0.769
BLG931.27.36745	0.7050	2.44	1.63	261.74489	-40.31792	11.633	0.0033	0.1113	0.0026	0.0105	1.456
GD1070.18.22288	45.1467	7.41	3.73	257.007546	-41.048747	11.369	0.0091	0.1362	0.0043	0.0049	1.031
LMC574.11.3407	0.2551	1.48	1.03	80.1415	-63.185667	16.919	0.0064	0.0989	0.0013	0.0092	0.454
LMC606.30.48	0.2698	1.67	1.11	92.27575	-63.376167	15.906	0.0141	0.1019	0.0038	0.0122	0.518
LMC751.15.2886	0.3753	1.70	1.16	98.082958	-66.307861	16.958	0.0090	0.1024	0.0012	0.0121	0.182
MBR108.18.3	0.2947	1.49	1.02	33.257292	-72.993167	13.376	0.0063	0.0989	0.0033	0.0128	1.097
MBR236.09.433	0.4398	1.51	1.07	50.642958	-80.540667	14.585	0.0024	0.0994	0.0028	0.0089	0.473
SMC711.22.1068	0.4466	2.35	1.56	9.833875	-70.378028	13.226	0.0029	0.1104	0.0053	0.0154	0.660
SMC720.28.40576	0.5674	4.29	2.56	11.938042	-73.13625	16.367	0.0017	0.1246	0.0037	0.0035	-
SMC742.26.330	0.3453	1.68	1.12	350.85925	-77.530417	13.864	0.0042	0.1020	0.0049	0.0074	1.074

Table 3.1: Selected objects together with period, estimated mass ratios, coordinates, Fourier coefficients (A_i) and parallax from Gaia DR3.

What should be emphasised here is the meaning of the BIC score. Little is assumed about objects; especially, the best fitting $\log g/Z$ is not investigated, which can be crucial to obtain a high quality spectral fit. Due to this effect, it is unreasonable to calculate the values of χ^2 and compare them between objects, as few of them can be better fitted with the given metallicity/ $\log g$ (for example ultraviolet observations can be sensitive not only to the temperature of the star but also to its metallicity). Even if some objects won't be accurately described, it is still possible to reliably assess if there are one or more stars contributing to the spectra. The SED fits together with light curves are presented in the Appendix A.

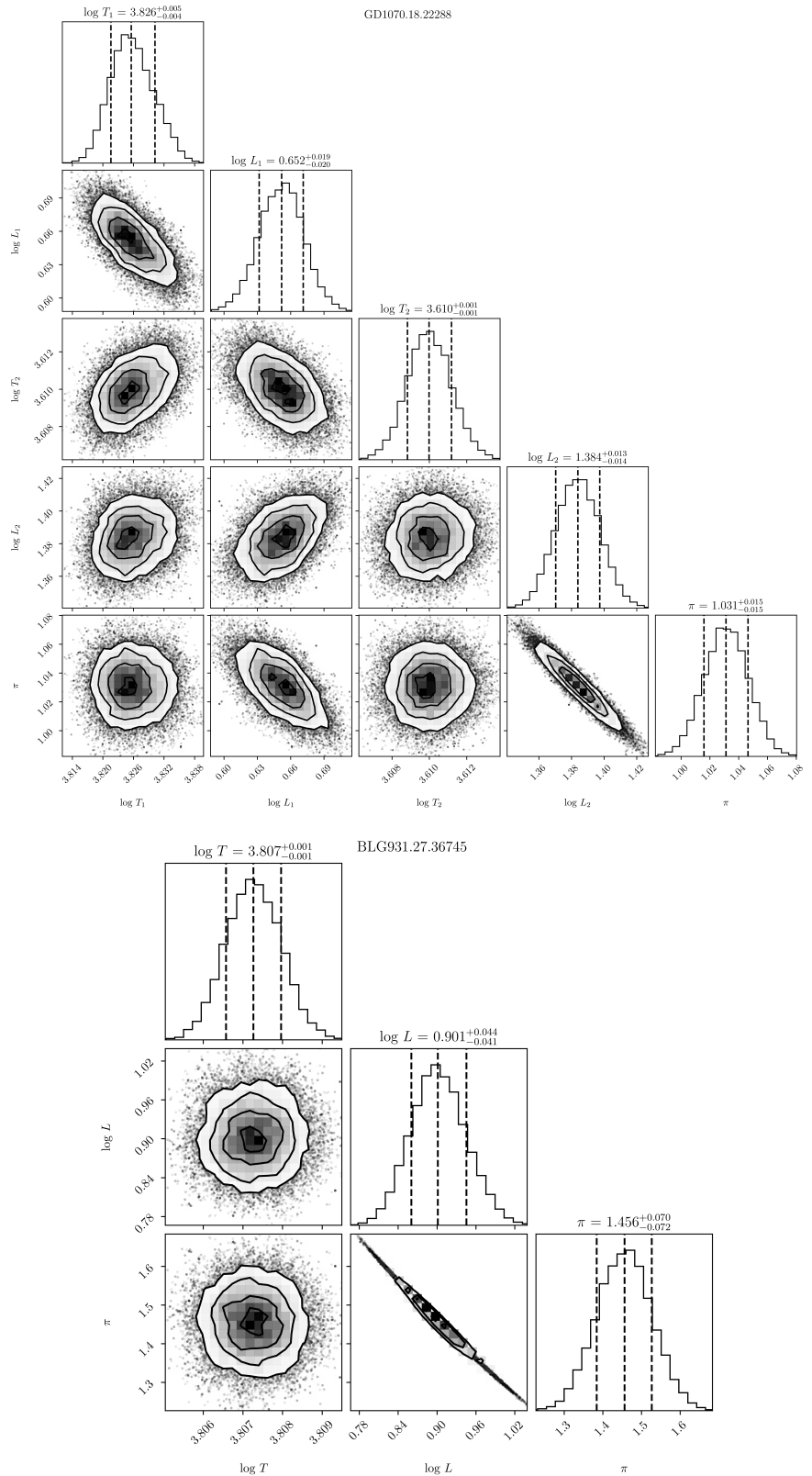


Figure 3.5: Posterior distribution from MCMC simulations for GD1070.18.22288 (double star model) and BLG931.27.36745 (single star model).

Chapter 4

Results

4.1. Physical parameters of objects

Each of the fourteen final objects was further investigated using available public data to determine the physical properties. Of all objects, twelve are spectral type G or F, one object is spectral type O, while the latter is composed of two stars. Thirteen stars from the list have a measured parallax from Gaia DR3 while one of the objects is located in the SMC.

The mass of each single object was estimated using the PARSEC (Bressan et al., 2012) evolutionary tracks. Assuming solar-like metallicity, simple approximate fits were obtained by choosing a best-fitting entry from the PARSEC track using temperature and luminosity estimates from SED fits. Each model was fitted with a track using the nearest metallicity from PARSEC data ($Z = 0.014$ in the case of objects inside the Galactic Disc and $Z = 0.004$ in the case of the SMC). As it was assumed that each object should be a MS star, parts of evolutionary tracks before the beginning of the ZAMS were discarded.

Name	T [K]	$\log_{10} L/L_\odot$	$E(B - V)$	d [kpc]	BIC	M_{PARSEC} [M_\odot]
BLG986.08.7	6190^{+26}_{-25}	$0.825^{+0.011}_{-0.012}$	0.226	0.83 ± 0.01	729.8	1.4
GD2246.03.18414	6974^{+21}_{-28}	0.806 ± 0.008	0.273	0.71 ± 0.01	586.3	1.45
GD1097.20.23000	6126 ± 13	$0.626^{+0.007}_{-0.006}$	0.221	0.56 ± 0.008	197.8	1.2
GD1448.27.17	8516^{+59}_{-64}	1.863 ± 0.013	0.611	1.30 ± 0.02	215.8	2.3
BLG931.27.36745	6416 ± 10	$0.901^{+0.044}_{-0.041}$	0.199	$0.69^{+0.04}_{-0.03}$	206.1	1.4
LMC574.11.3407	4740 ± 24	$-0.349^{+0.153}_{-0.124}$	0.034	$2.21^{+0.42}_{-0.29}$	849.3	–
LMC606.30.48	5516 ± 25	-0.053 ± 0.066	0.047	$1.93^{+0.15}_{-0.13}$	184	0.85
LMC751.15.2886	6068 ± 23	$0.392^{+0.342}_{-0.241}$	–	$5.39^{+2.60}_{-1.31}$	470.3	1.1
MBR108.18.3	5884 ± 6	0.228 ± 0.011	–	0.91 ± 0.01	3333.3	1.0
MBR236.09.433	6471 ± 10	0.717 ± 0.027	–	2.12 ± 0.07	592.1	1.35
SMC711.22.1068	6771 ± 5	$0.852^{+0.017}_{-0.015}$	0.021	1.52 ± 0.03	707.4	1.45
SMC720.28.40576	34079^{+536}_{-496}	$4.366^{+0.069}_{-0.071}$	0.095	–	168.8	16
SMC742.26.330	5808 ± 6	0.356 ± 0.010	–	0.93 ± 0.01	2539.4	1

Table 4.1: Estimated physical parameters of objects using the single star model together with PARSEC mass estimates and extinction estimates.

4.2. Radial velocity semiamplitude estimation from Gaia DR3 data

Half of the objects in the final list have available high-quality radial velocity information that is normally computed for bright stars from the Gaia DR3 catalogue. While the estimate of the radial velocity is based on the median of measurements, the error of this estimate is based on the epoch standard deviation. According to Katz et al. (2022) the radial velocity error δv is calculated via the equation

$$\delta v = \sqrt{\sigma_{med}^2 + 0.11^2} \quad (4.1)$$

$$\sigma_{med} = \sqrt{\frac{\pi}{2}} \frac{\sigma}{\sqrt{N}} \quad (4.2)$$

where σ is a standard deviation of the radial velocity and N stands for a number of transits used to compute radial velocity. This simple formula allows to obtain variance of radial velocity measurements as

$$\sigma^2 = \frac{2N}{\pi} ((\delta v)^2 - 0.11^2). \quad (4.3)$$

It can be proven (for details see Appendix B) that if one assumes that the error is dominated by a sinusoidal radial movement with a semi-amplitude K , a variance of velocity is equal to

$$\sigma^2 = \frac{K^2}{2}. \quad (4.4)$$

This observation can be used to estimate a semi-amplitude of the radial velocity using Gaia measurements (denoted from here as K_{Gaia}) as

$$K_{Gaia} = \sqrt{\sigma^2} \sqrt{2} = 2 \sqrt{\frac{N}{\pi} ((\delta v)^2 - 0.11^2)} \quad (4.5)$$

This radial velocity amplitude is used then to calculate a binary mass function, which provides a lower limit on the companions mass, and can be obtained using the equation

$$f(M_1, M_2, i) = \frac{M_2^3 \sin i^3}{(M_1 + M_2)^2} = \frac{K^3 P}{2\pi G}, \quad (4.6)$$

where P denotes a orbital period, while G is the gravitational constant. For each object with a radial velocity estimate, a mass function was obtained and presented in the table 4.2 with other relevant parameters. For each object with a PARSEC mass estimate, a lower boundary of a companion mass was calculated by solving equation 4.6 with $\sin(i) = 1$ and placed in the table as M_{min} .

In Katz et al. (2022) a criterion was presented that allows to test whether an object is variable in radial velocity, based on values of rv_chisq_pvalue and $rv_renormalised_gof$. The criterion states that objects with $N > 10$, $T_{eff} \in [3900, 8000]$ K, $rv_chisq_pvalue < 0.01$ and $rv_renormalised_gof > 4$ can be safely considered to be variable in radial velocity. Each candidate was tested using the described method, and only two entries (BLG931.27.36745 and GD1097.20.23000) cannot be safely assumed to be variable in radial velocity as they were not observed enough times. This observation is the first good sign that selected candidates really are binary in nature and the sample is not polluted, i.e. by pulsating stars.

Name	Period [d]	RV [km/s]	N	δv [km/s]	K_{Gaia} [km/s]	$f(M_1, M_2, i)$ [M_\odot]	M_{min} [M_\odot]
GD2246.03.18414	0.4270	27.68	25	23.03	129.93	0.097	0.79
GD1097.20.23000	0.4570	36.5	10	21.03	75.03	0.020	0.37
BLG986.08.7	0.5132	-1.69	15	18.11	79.14	0.026	0.43
BLG931.27.36745	0.7050	-4.35	8	14.81	47.26	0.0077	0.28
GD1448.27.17	1.2410	33.08	22	7.69	40.69	0.0086	0.40
GD1070.18.22288	45.1467	38.71	20	7.66	38.65	0.27	-

Table 4.2: Estimated mass functions together with other relevant parameters.

4.3. Detailed analysis of objects

In this section, a detailed characteristic of individual objects is provided. It is divided into 3 subsections, where the first two will quickly cover the information available for objects GD1070.18.22288 and SMC720.28.40576 while the third is dedicated to the remaining ones.

4.3.1. GD1070.18.22288

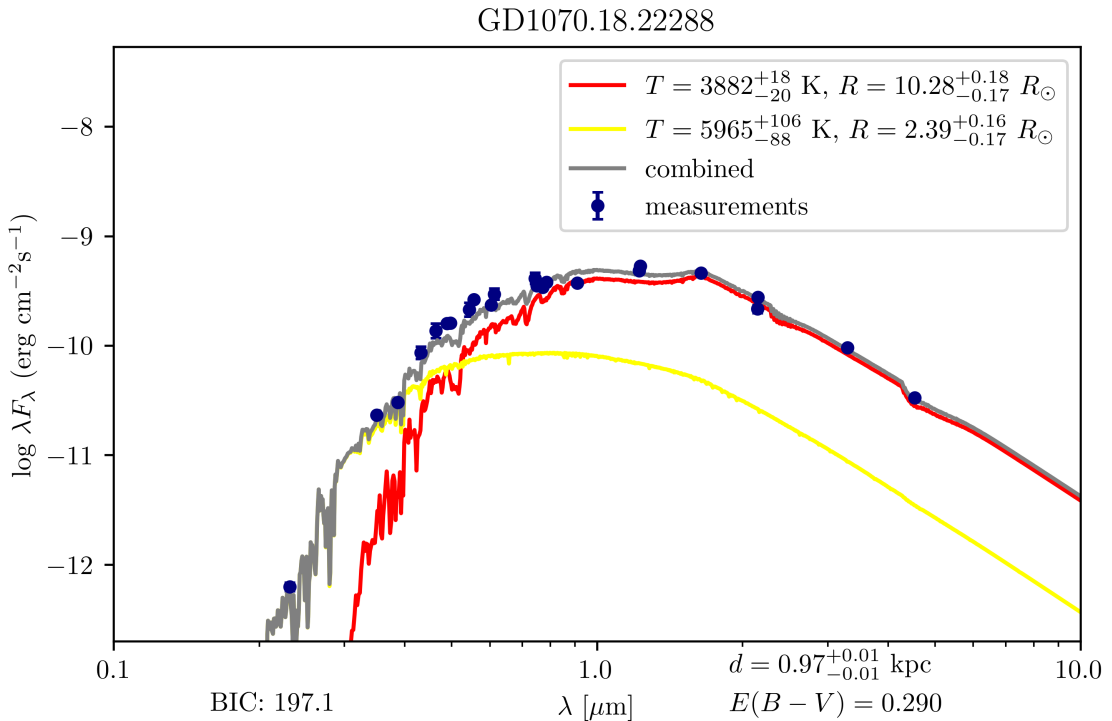


Figure 4.1: Spectral Energy Distribution fit for GD1070.18.22288 using a model with two components.

GD1070.18.22280 has the longest period compared to other selected objects with $P \approx 45$ d and was listed as a plausible candidate only because of the reported X-ray emission. Due to an excess amount of observations in many parts of the spectra it was possible to obtain a high-quality spectral energy distribution fit that revealed two sources with different temperatures;

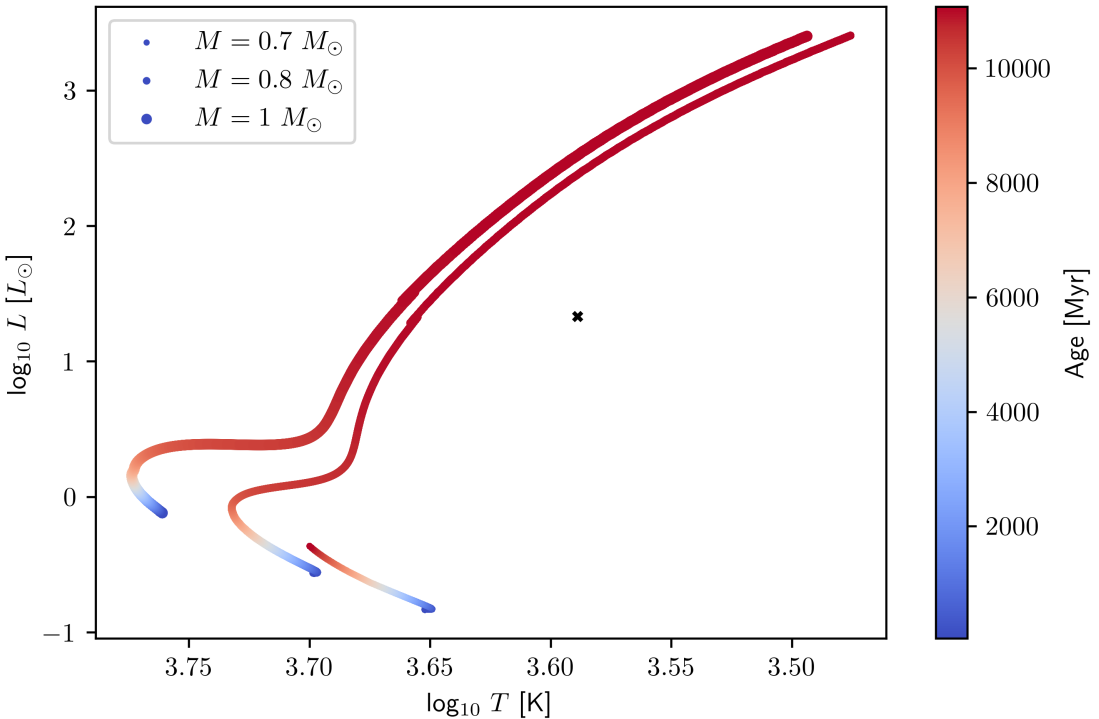
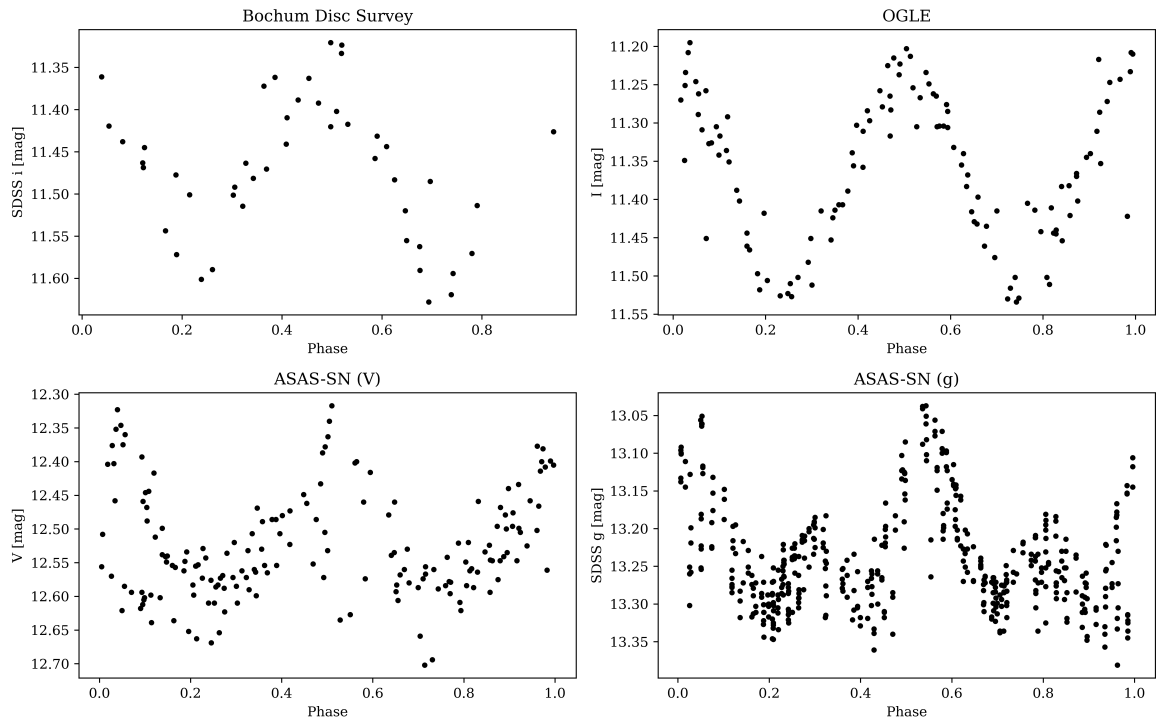


Figure 4.2: Nearest evolutionary tracks for the cold component of GD1070.18.22288.

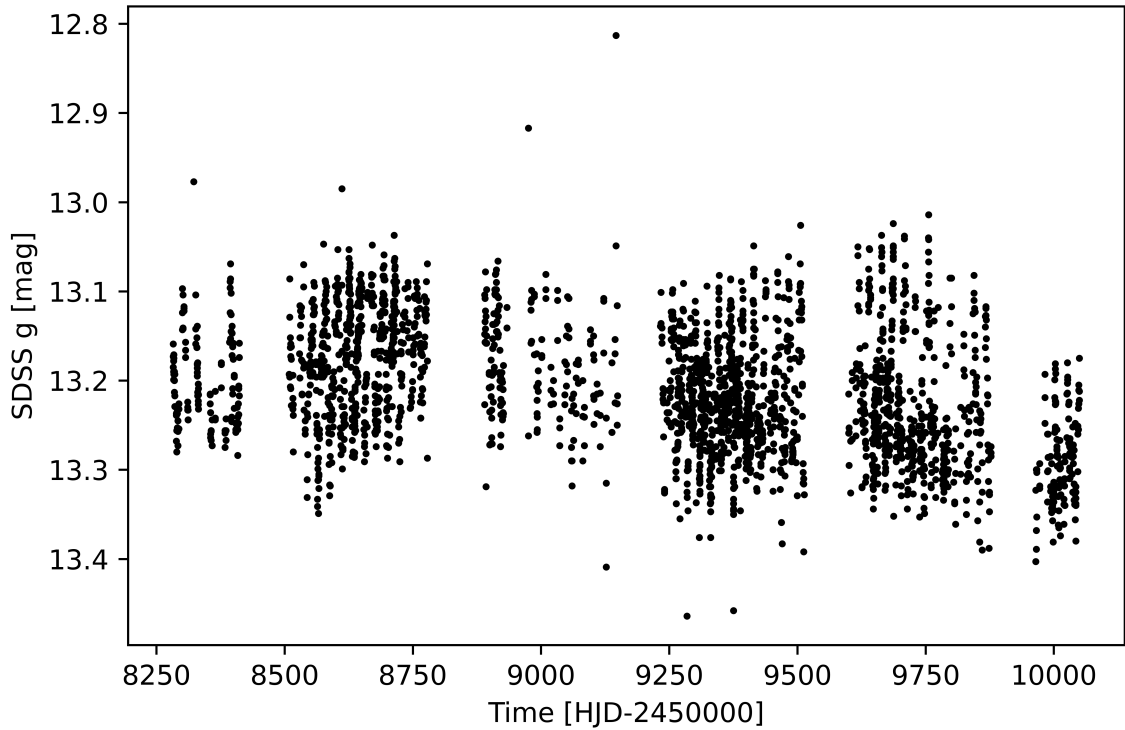
detailed distribution can be seen in the figure 4.1. One of the objects with a rather low effective temperature of $T \approx 3800$ K has radius $R \approx 10 R_{\odot}$ and was quite far from any evolutionary track in the PARSEC database. This can indicate that was stripped in the past by its companion. The position of the cold companions in the HR diagram is presented in the figure 4.2. The object can also be found in the ASAS-SN database (Jayasinghe et al., 2019) under the identification number J170801.81-410255.6 where it is classified as a rotational variable star with half of the period found in this work. The ASAS-SN observed it in the V and SDSS g bands, allowing light curves to be compared with the OGLE one. Furthermore, the object was observed in the SDSS i band by the Bochum Galactic Disk Survey (Hackstein et al., 2015). The comparison between all light curves can be found in the graph 4.3a. ASAS-SN observations in the g band can be traced back to 2016 and allow one to gain a better understanding of the nature of the object. The evolution of the light curve over time is presented in the graph 4.3b.

GD1070.18.22288 was observed in the X-ray by Swift and XMM missions and published in serendipitous sources catalogues (Evans et al. (2020) and Traulsen et al. (2020)) with id names J170801.8-410254 and J170801.8-410255 respectively. The angular distance between the position reported by the XMM DR11 catalogues (Traulsen et al., 2020) and the OGLE position is $0.105''$, three times less than the positional error reported by XMM ($0.365''$). The XMM X-ray source was observed few times and is transient in nature, changing its flux slightly across time. This area of the galactic disc also came to attention because of the gamma-ray source HESS J1708-410 (Aharonian et al., 2008) located $4.212'$ from the estimated OGLE position. Gamma emission from the source has an extended character, and the position reported by the OGLE falls near the 1σ region of the emission centre. To date no plausible explanation for the origin of the aforementioned source was found despite multiple efforts and

GD1070.18.22288



(a) Light curve of GD1070.18.22288 in 4 different bands folded with the OGLE period.



(b) Change in brightness in the SDSS g band over time.

search in various parts of the optical spectra. One particular work (Van Etten et al., 2009) observed a close vicinity of the gamma-ray source and found emission from the point source labelled in the publication as nr 1 (hereinafter referred to as [VFH2009] 1). This particular point source, although quite faint, coincides with the position of GD1070.18.22280 with an accuracy of $0.382''$. In the publication it was found that X-ray emission is best fitted with an absorbed power law by hydrogen density $n_H = 2.0 \times 10^{21} \text{ cm}^{-2}$. Interestingly, the assumed distance of 3 kpc based on radio observations is nearly three times higher than value obtained using the parallax from the Gaia DR3. The X-ray luminosity based on the Gaia parallax for different times roughly lies in the range $L_X = (1 - 3) \cdot 10^{31} \text{ erg/s}$.

As one can see in the figure 4.3a there is a discrepancy between the curves in the I band and the curves from ASAS-SN. This discrepancy can be explained after investigation when light curves were collected. The OGLE light curve is composed of observations collected from 2456467 to 2458734 HJD, but most samples were collected before 2457201 HJD. On the other hand, ASAS-SN observations were collected in the g band after 2459797 HJD. Based on ASAS-SN archive data, there is a visible change around 2459100 when the period decreases from ~ 45 d to nearly half the value around ~ 22.4 d. This observation, together with the evolution of the amplitude of the variability as presented in the figure 4.3b, suggests that the object represents a class of rotational variables. This can also be partially supported by the X-ray emission from the system; it is widely known that many rotational variables like RS Canum Venaticorum can emit X-rays with a luminosity around $\sim 10^{31} \text{ erg/s}$ (Walter et al., 1980), so the value obtained from XMM is consisted with emission from this type of system. It is hard to determine whether the OGLE curve exhibits changes in brightness similar to the ASAS-SN light curve, as observations cover only a relatively short period of time. It is highly unlikely that the variability in the I band is caused by the ellipsoidal modulation. If the period would be equal to 45 d, the inferred radii would be too small for the system to fill their Roche Lobes (unless the system would have very small total mass). The most plausible explanation states that the system is similar to the RS Canum Venaticorum variable, undergoing mass transfer in the past. The colder star is covered in spots that emerge due to high magnetic fields; such stars can develop powerful coronal heating responsible for the X-ray emission. One could investigate the X-ray spectrum of an object to find whether it is consisted with the emission from the hot plasma, since although the object does not represent a class of ellipsoidal variables this line of investigation is dropped as it is beyond scope of the work.

4.3.2. SMC720.28.40576

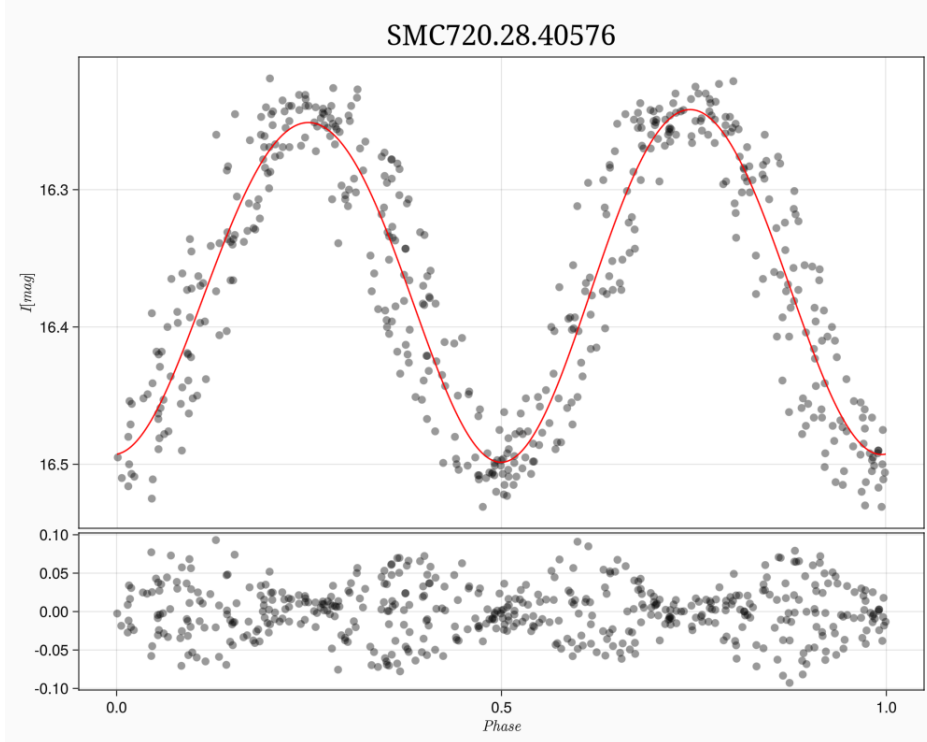


Figure 4.4: Light curve of SMC720.28.40576 collected by the OGLE project.

SMC720.28.40576 is the only object in the sample that is probably located in Magellanic Clouds as the measured parallax is statistically unsignificant. The SED fit estimate suggest the star to be spectral type O, measured magnitudes with the best-fitting spectra are presented in the figure 4.5. The estimated period of the variable is nearly half of the day; such a short period suggests a very compact setup of stars. The PARSEC evolutionary track estimates the mass of the object to be around $16 M_{\odot}$. Star was published already in Pawlak et al. (2016) and classified as a contact binary. Although no companion is visible in the SED distribution, it might hide itself in the light of a primary star. No WISE source could be found, as the nearest detection is nearly 10 arcsec away from the position; lack of any observations in W3 and W4 bands is very problematic as they allow to probe object in low temperatures.

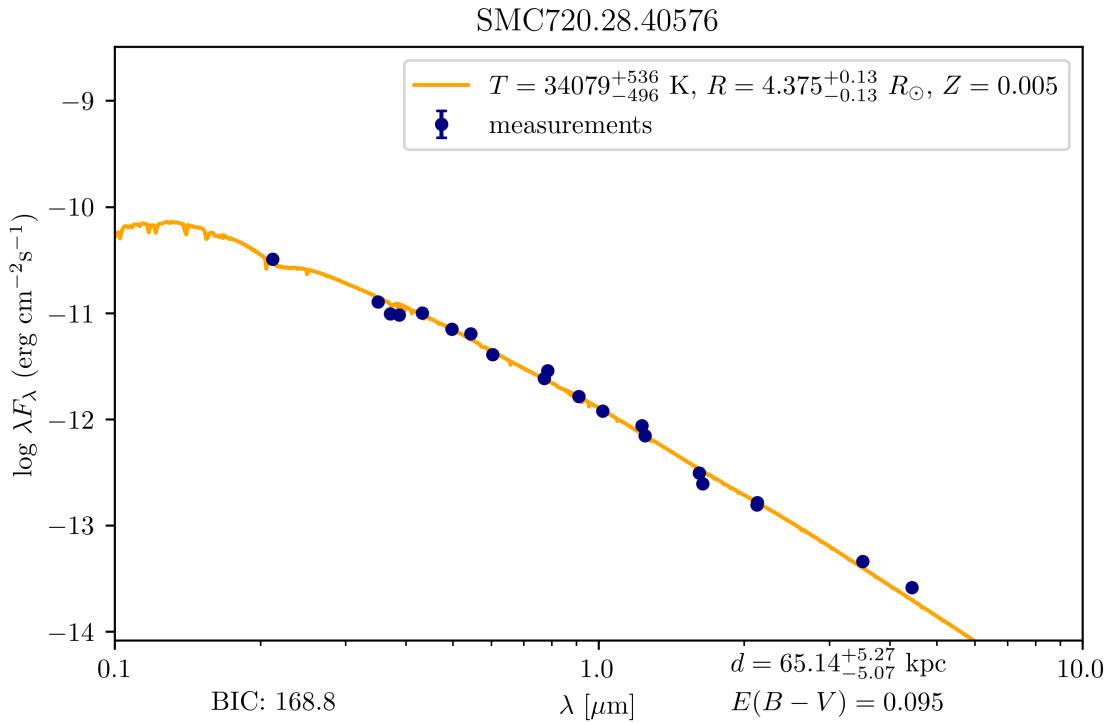


Figure 4.5: Single model SED fit for SMC720.28.40576.

The available data paired with the MCMC approach allow one to put some constraints on parameters of objects even if the chain had not converged. When the MCMC chain is not able to determine the significance of some parameters, it is reconstructing the prior distribution. If for some set of parameters predicted probability is very small such region shouldn't be populated by samples, resulting in the uniformly populated region, where possible companion star can reside. The second MCMC run was performed and 64000 samples were drown from the posterior distribution with 32 walkers. The SED fit is performed assuming $\log g_1 = 4$ and $\log g_2 = 4$, since one expects the secondary component to be the main sequence star. The results of the MCMC sampling were plotted on samples from the HYG database¹ and are presented in the figure 4.6

¹<https://www.astronexus.com/hyg>

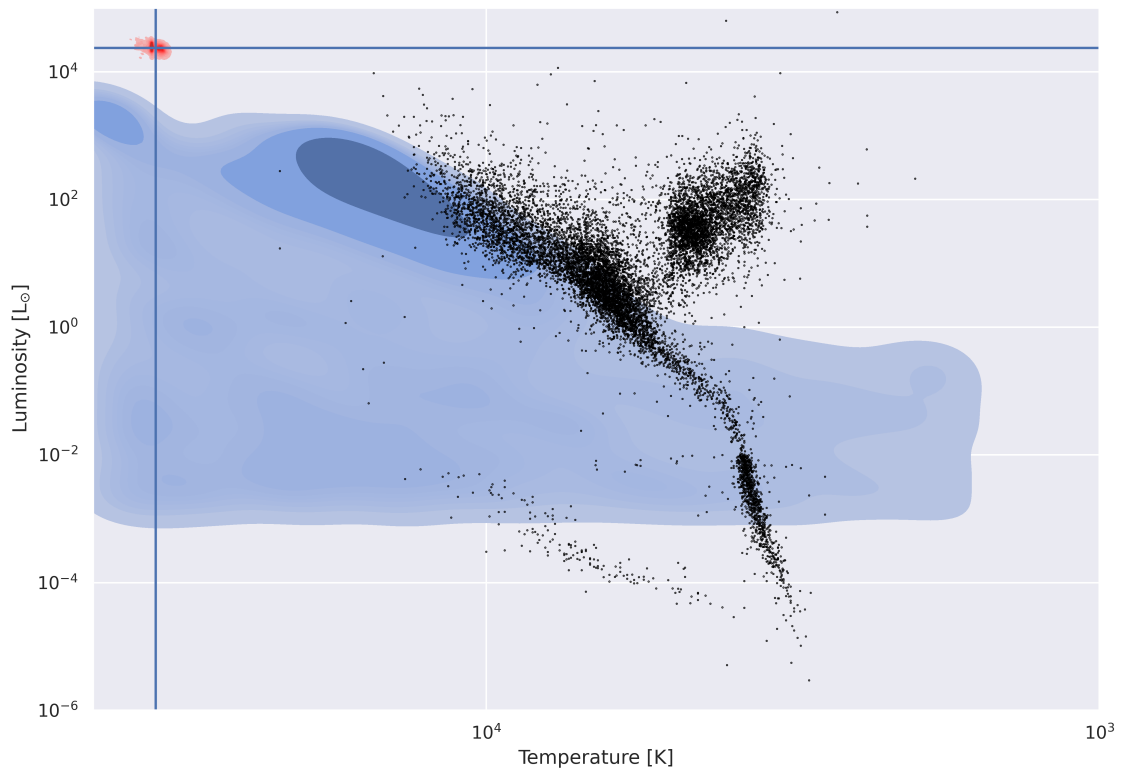


Figure 4.6: The posterior estimate for the parameters of SMC720.28.40576 highlighted in red (primary component) and blue (secondary component).

One can see that samples fill the space almost uniformly, but omit regions populated with cold and luminous stars, as those are too luminous in the infrared to reproduce observed values. Although any object on the giant branch can be ruled out, many regions on the HR diagram can host a potential secondary companion. Most importantly, main sequence stars cannot be ruled out as they are to faint compared to the primary object.

4.3.3. Remaining objects

The majority of objects in the list can be characterised as objects with intermediate temperature. They typically have a radius in order of few solar radii and spectral type from G to A. Although no detailed information about objects was found in the literature, two of them are listed as nonsingle stars in the Gaia DR3 Eclipsing Binaries catalogue (BLG986.08.7, BLG931.27.36745). The catalogue contains stars with collected light curves that matched the precomputed set of eclipsing/ellipsoidal binaries. Detailed processing steps can be found in the Gaia documentation¹. As part of Gaia preprocessing, the light curve is matched with the precomputed set, then the best model serves as a starting point in the local optimiser trying to refine the solution further. The model is solved with respect to the parameters:

- fillout factors of stars s_1 , s_2 ,
- inclination i ,
- temperature ratio T_1/T_2 (effective values),
- argument of periastron ω ,
- time t_0 of eclipse.

Both objects reported by Gaia DR3 are fitted with the contact binary model where $s_1 > 1$ and $s_2 > 1$ with almost no temperature difference (ratio close to 1). This result pointed out that it is possible to obtain similar results with the contact system of two simillar stars. In such compact setup stars are in thermal equilibrium so they are able to fool the SED as they are well fitted with the single star model.

This line of inquiry was further investigated, and objects were fitted using the PHOEBE simulation software (Wilson & Devinney (1971),Prša & Zwitter (2005),Conroy et al., (2020)). The model was constructed in such a way that both stars shared the temperature T (inferred from a single model SED) and were overflowing their Roche lobes. Only objects from the galactic disc sample were analysed as it is possible to compare estimates of radial velocity semiamplitude with values from the light-curve modelling. Two masses together with an inclination i and a radius of the primary star R_1 form four parameters, which are fitted to minimise the χ^2 value using the Nelder-Mead algorithm. The second radius is no longer a free parameter, as it is controlled by a common envelope. In the study no flux normalisation was performed, the distance and the extinction were set on the basis of the values used to perform the spectral energy distribution fit. One could infere effective luminosity of both stars from a SED fit although it should be noted, that a mean luminosity of elispoidal binary is always smaller then a sum of a luminosity of both stars. Hence, in order to get more realistic model, the total luminosity of the system (parametrised by the radius of primary star) can be changed. The fitted values together with the χ^2 values are presented in the table 4.3 together with the predicted semiamplitude of the velocity and the estimated one. An example light curve fit for the object BLG931.27.36745 can be seen in the plot 4.7a.

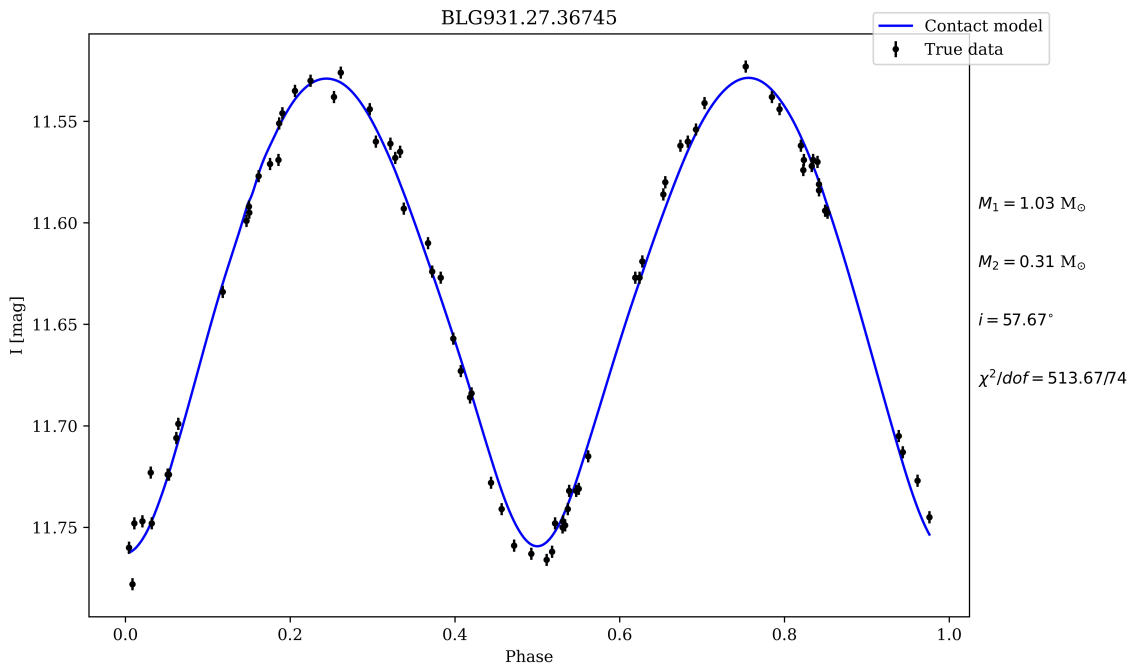
¹https://gea.esac.esa.int/archive/documentation/GDR3/Data_analysis/chap_cu4nss/sec_cu4nss_eclipsing_bin/

Name	M_1 [M_\odot]	M_2 [M_\odot]	R_1 [R_\odot]	R_2 [R_\odot]	i	K_{estimate} [km/s]	K_{Gaia} [km/s]	χ^2/dof
BLG931.27.36745	1.03	0.31	1.88	1.21	57.67°	50.71	47.26	513.67/74
GD1097.20.2300	1.14	0.37	1.56	1.02	55.74°	64.05	75.03	2929.66/118
BLG986.08.7	1.43	0.43	1.82	1.15	46.52°	55.17	79.14	827.58/72
GD2246.03.1814	1.09	0.34	1.45	0.92	50.63°	58.42	129.93	1426.90/124
GD1448.27.17	1.58	0.75	2.99	2.16	55.39°	69.52	40.69	4391.59/184

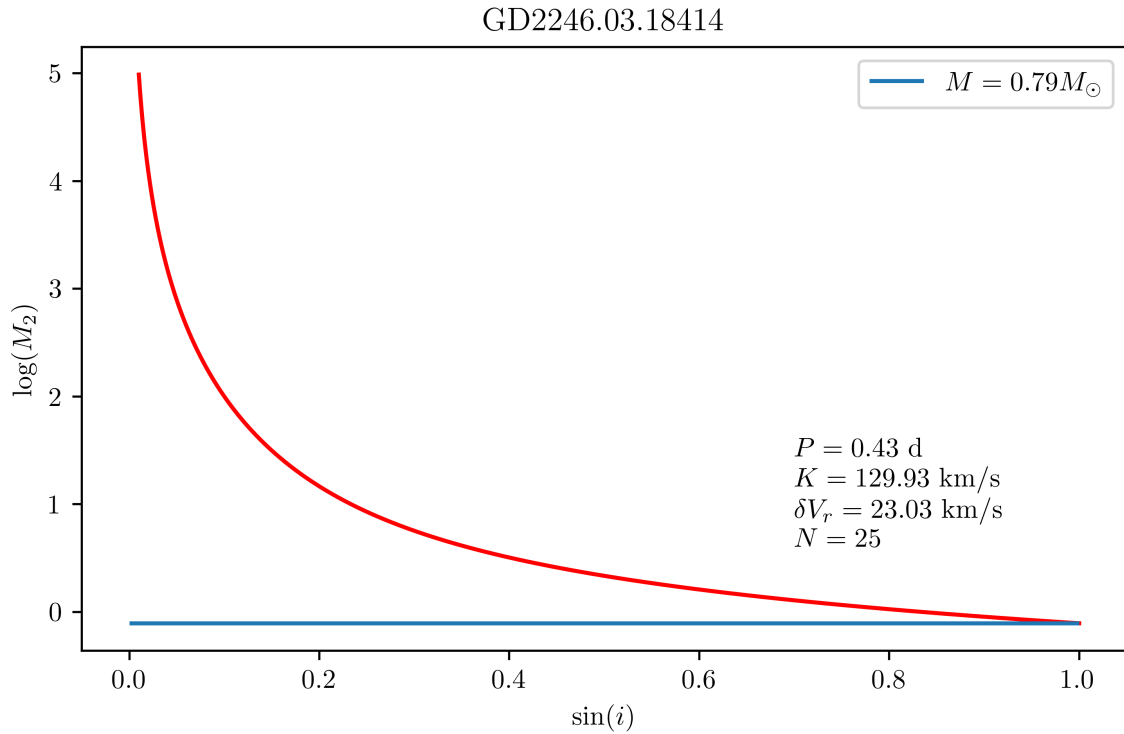
Table 4.3: Parameters used to fit the light curves of objects together with the estimates of radial velocities and the normalised χ^2 values.

Few of the light curves can be well fitted by using the contact light curve model. Objects BLG931.27.36745 or BLG986.08.7 not only match fitted values very well but also predicted velocity semi-amplitudes are comparable to those estimated from the Gaia DR3 release. In some cases like GD1097.20.2300 or GD1448.27.17 there is some room for improvement; there are some discrepancies between the model and observed curves. The most puzzling object in the whole sample is GD2246.03.1814, despite the fact that light curve modelling gave quite satisfying result, the predicted value of velocity semi-amplitude is twice that of the value estimated using Gaia data. Moreover, the amplitude of radial velocity measured by the Gaia mission is equal 410.92 km/s questioning the previous estimate of radial velocity. This can be explained either by an eccentric orbit of the star or by outlier measurements that were not removed as part of a preprocessing. If this value is correct and if one assumes mass of the primary star from the PARSEC fit, the lower bound for the companion's mass is $\sim 0.8 M_\odot$, detailed dependence between $\sin(i)$ and M_2 is presented in the figure 4.7b. Hence, GD2246.03.1814 is potentially most promising candidate for a dormant compact companion.

The values obtained from the fit can be quite distant from the reality, as there is not enough data to constrain the parameters of the model. Despite this fact, as demonstrated, not only some of the objects can be well described using the contact model, but in all cases contact model can achieve an amplitude comparable to the real one. This makes such binaries one of the great weaknesses of the method described in Gomel et al. (2021b) as a simple contact binary can easily be classified as a potential candidate.



(a) The light curve fit with the contact binary model for BLG931.27.36745.



(b) Dependence between the companion mass and the binary inclination for GD2246.03.1814.

Chapter 5

Discussion & Conclusions

Of the total 8515 objects investigated in this study, only fourteen were classified as plausible candidates for compact companion binaries. Only one object in the sample is probably located in Magellanic Clouds while rest of them reside inside the Milky Way. This is not unexpected as after limiting $I < 17$ mag only most luminous objects can pass this threshold. Further investigation into the sample revealed one rotational variable and suggested an alternative explanation for twelve objects in the form of contact binaries with an intermediate mass ratio. It is impossible to pinpoint exact nature of objects as only spectroscopic observations allow to determine radial velocities of stars and true nature of companion objects. All of those candidates can potentially host neutron stars/black holes, but due to great amounts of contact binaries in the universe probability contact scenario seem to be much more plausible. Gaia DR3 semiamplitude estimations suggest most of the companion's are not compact at all, even for stars with the estimated radial velocity amplitude ~ 100 km/s the companion's mass lower bound is too low for compact star. Only one object distinguishes itself from the rest with the high estimate of the velocity semiamplitude ≈ 120 km/s, which is difficult to explain with a simple contact binary model. Based on the PARSEC estimate, a lower bound for companion mass is equal $\approx 0.8 M_{\odot}$ making the candidate quite promising.

Until now, only one publication tried to perform any kind of follow-up observations of candidates described in Gomel et al. (2022) (also found with the method described in Gomel et al. (2021b)). Nagarajan et al. (2023) selected sample of objects that were promising and obtained epochal radial velocities for them. It was found that all selected objects cannot host any type of compact object as the velocity semiamplitudes are too low. It was suggested that such variables can be easily explained by contact binaries with or without spots. This conclusion is similar in some sense to the results presented in this work. Such an explanation is quite convincing as such objects should be quite common contrary to the black hole binaries. It was pointed out that stars with the nearly overflowing primary star should be rather rare as this phase of a binary evolution is very shortlived. Hence, system should be either well-detached or overflowing its Roche lobe, resulting in an X-ray binary. In fact in Gomel et al. (2021b) the method presented was applied to some X-ray binaries with black hole companions and found that at least some of them would be detected. As noted in the introduction, the creation of such systems is rather rare, so potential sample of black holes that can be revealed seem to be small compared to black holes in wider binaries. Moreover, as demonstrated, a simple contact model can be easily classified as a candidate. Therefore, the potential sample can be primarily populated by those common false positive contaminants. Although Nagarajan et al. (2023) did not find any compact companion, more objects should be investigated to better characterise the population of these high-amplitude binaries.

Bibliography

- Aharonian F., et al., 2008, *Astronomy & Astrophysics*, 477, 353
- Astropy Collaboration et al., 2022, *The Astrophysical Journal*, 935, 167
- Belczynski K., Wiktorowicz G., Fryer C. L., Holz D. E., Kalogera V., 2012, *The Astrophysical Journal*, 757, 91
- Belloni T. M., Motta S. E., 2016, in Bambi C., ed., , Vol. 440, *Astrophysics of Black Holes*. Springer Berlin Heidelberg, Berlin, Heidelberg, pp 61–97, doi:10.1007/978-3-662-52859-4_2, http://link.springer.com/10.1007/978-3-662-52859-4_2
- Bianchi L., Herald J., Efremova B., Girardi L., Zabot A., Marigo P., Conti A., Shiao B., 2011, *Astrophysics and Space Science*, 335, 161
- Bovy J., Rix H.-W., Green G. M., Schlafly E. F., Finkbeiner D. P., 2016, *The Astrophysical Journal*, 818, 130
- Bressan A., Marigo P., Girardi L., Salasnich B., Dal Cero C., Rubele S., Nanni A., 2012, *Monthly Notices of the Royal Astronomical Society*, 427, 127
- Brown G. E., Bethe H. A., 1994, *The Astrophysical Journal*, 423, 659
- Cardelli J. A., Clayton G. C., Mathis J. S., 1989, *The Astrophysical Journal*, 345, 245
- Cioni M.-R., et al., 2000, *Astronomy and Astrophysics Supplement Series*, 144, 235
- Cioni M. R. L., et al., 2017, *VizieR Online Data Catalog*, p. II/351
- Claret A., 2000, *Astronomy and Astrophysics*, 363, 1081
- Collaboration G., et al., 2022,] 10.48550/ARXIV.2208.00211
- Conroy K. E., et al., 2020, *The Astrophysical Journal Supplement Series*, 250, 34
- Corral-Santana J. M., Casares J., Muñoz-Darias T., Bauer F. E., Martínez-Pais I. G., Russell D. M., 2016, *Astronomy & Astrophysics*, 587, A61
- Cutri R. M., et al., 2021, *VizieR Online Data Catalog*, p. II/328
- Denis C., 2005, *VizieR Online Data Catalog*, p. B/denis
- Drimmel R., Cabrera-Lavers A., Lopez-Corredoira M., 2003, *Astronomy & Astrophysics*, 409, 205
- Eggleton P. P., 1983, *The Astrophysical Journal*, 268, 368

- El-Badry K., et al., 2022, Monthly Notices of the Royal Astronomical Society, 518, 1057
- El-Badry K., et al., 2023, A red giant orbiting a black hole, <http://arxiv.org/abs/2302.07880>
- Engel M., Faigler S., Shahaf S., Mazeh T., 2020, Monthly Notices of the Royal Astronomical Society, 497, 4884
- Evans P. A., et al., 2020, The Astrophysical Journal Supplement Series, 247, 54
- Foreman-Mackey D., 2016, The Journal of Open Source Software, 1, 24
- Foreman-Mackey D., Hogg D. W., Lang D., Goodman J., 2013, Publications of the Astronomical Society of the Pacific, 125, 306
- Gaia Collaboration et al., 2018, Astronomy & Astrophysics, 616, A1
- Ginsburg A., et al., 2019, The Astronomical Journal, 157, 98
- Gomel R., Faigler S., Mazeh T., 2021a, Monthly Notices of the Royal Astronomical Society, 501, 2822
- Gomel R., Faigler S., Mazeh T., 2021b, Monthly Notices of the Royal Astronomical Society, 504, 2115
- Gomel R., Faigler S., Mazeh T., Pawlak M., 2021c, Monthly Notices of the Royal Astronomical Society, 504, 5907
- Gomel R., et al., 2022, Astronomy & Astrophysics
- Gordon K. D., et al., 2011, The Astronomical Journal, 142, 102
- Green G. M., Schlafly E., Zucker C., Speagle J. S., Finkbeiner D., 2019, The Astrophysical Journal, 887, 93
- Greiner J., Cuby J. G., McCaughrean M. J., 2001, Nature, 414, 522
- Hackstein M., et al., 2015, Astronomische Nachrichten, 336, 590
- Henden A. A., Levine S., Terrell D., Welch D. L., 2015, 225, 336.16
- Jacyszyn-Dobrzeniecka A. M., et al., 2016, Acta Astronomica, 66, 149
- Jayasinghe T., et al., 2019, Monthly Notices of the Royal Astronomical Society
- Katz D., et al., 2022, Gaia Data Release 3 Properties and validation of the radial velocities, <http://arxiv.org/abs/2206.05902>
- Kopal Z., 1959, Close binary systems. <https://ui.adsabs.harvard.edu/abs/1959cbs..book.....K>
- Kreidberg L., Bailyn C. D., Farr W. M., Kalogera V., 2012, The Astrophysical Journal, 757, 36
- Kruszyńska K., et al., 2022, Astronomy & Astrophysics, 662, A59
- Langer N., et al., 2020, Astronomy & Astrophysics, 638, A39

- Lasota J.-P., 2001, New Astronomy Reviews, 45, 449
- Lejeune T., Cuisinier F., Buser R., 1998, Astronomy and Astrophysics Supplement Series, 130, 65
- Lennon D. J., Dufton P. L., Villaseñor J. I., Evans C. J., Langer N., Saxton R., Monageng I. M., Toonen S., 2022, *Astronomy & Astrophysics*, 665, A180
- Liu J., et al., 2019, *Nature*, 575, 618
- Loeb A., Gaudi B. S., 2003, *The Astrophysical Journal*, 588, L117
- Masuda K., Hotokezaka K., 2019, *The Astrophysical Journal*, 883, 169
- McMahon R. G., Banerji M., Gonzalez E., Koposov S. E., Bejar V. J., Lodieu N., Rebolo R., VHS Collaboration 2021, *VizieR Online Data Catalog*, p. II/367
- Meixner M., et al., 2006, *The Astronomical Journal*, 132, 2268
- Minniti D., Lucas P., VVV Team 2017, *VizieR Online Data Catalog*, p. II/348
- Morris S. L., Naftilan S. A., 1993, *The Astrophysical Journal*, 419, 344
- Nagarajan P., El-Badry K., Rodriguez A. C., van Roestel J., Roulston B., 2023, Spectroscopic follow-up of black hole and neutron star candidates in ellipsoidal variables from Gaia DR3, <http://arxiv.org/abs/2304.07324>
- Onken C. A., et al., 2019, *Publications of the Astronomical Society of Australia*, 36, e033
- Page M. J., et al., 2012, *Monthly Notices of the Royal Astronomical Society*, 426, 903
- Pawlak M., et al., 2016, *Acta Astronomica*, 66, 421
- Prša A., Zwitter T., 2005, *The Astrophysical Journal*, 628, 426
- Sahu K. C., et al., 2022, *The Astrophysical Journal*, 933, 83
- Sajadian S., Sahu K. C., 2023, *The Astronomical Journal*, 165, 96
- Schwarzenberg-Czerny A., 1989, *Monthly Notices of the Royal Astronomical Society*, 241, 153
- Shenar T., et al., 2022, *Nature Astronomy*, 6, 1085
- Skowron D. M., et al., 2021, *The Astrophysical Journal Supplement Series*, 252, 23
- Skrutskie M. F., et al., 2006, *The Astronomical Journal*, 131, 1163
- Soszyński I., et al., 2016, *Acta Astronomica*, 66, 131
- Spitzer Science C., 2009, *VizieR Online Data Catalog*, p. II/293
- Thompson T. A., et al., 2019, *Science*, 366, 637
- Traulsen I., et al., 2020, *Astronomy & Astrophysics*, 641, A137
- Udalski A., Szymanski M., Kaluzny J., Kubik M., Mateo M., 1992, *Acta Astronomica*, 42, 253

- Udalski A., Szymański M. K., Szymański G., 2015, OGLE-IV: Fourth Phase of the Optical Gravitational Lensing Experiment, <http://arxiv.org/abs/1504.05966>
- Van Etten A., Funk S., Hinton J., 2009, The Astrophysical Journal, 707, 1717
- Walter F. M., Cash W., Charles P. A., Bowyer C. S., 1980, The Astrophysical Journal, 236, 212
- Wilson R. E., Devinney E. J., 1971, The Astrophysical Journal, 166, 605
- Wolf C., et al., 2018, Publications of the Astronomical Society of Australia, 35, e010
- Wright E. L., et al., 2010, The Astronomical Journal, 140, 1868
- Zaritsky D., Harris J., Thompson I. B., Grebel E. K., Massey P., 2002, The Astronomical Journal, 123, 855
- Zaritsky D., Harris J., Thompson I. B., Grebel E. K., 2004, The Astronomical Journal, 128, 1606
- Zwart S. F. P., Verbunt F., Ergma E., 1997, The formation of black-holes in low-mass X-ray binaries, <http://arxiv.org/abs/astro-ph/9701037>

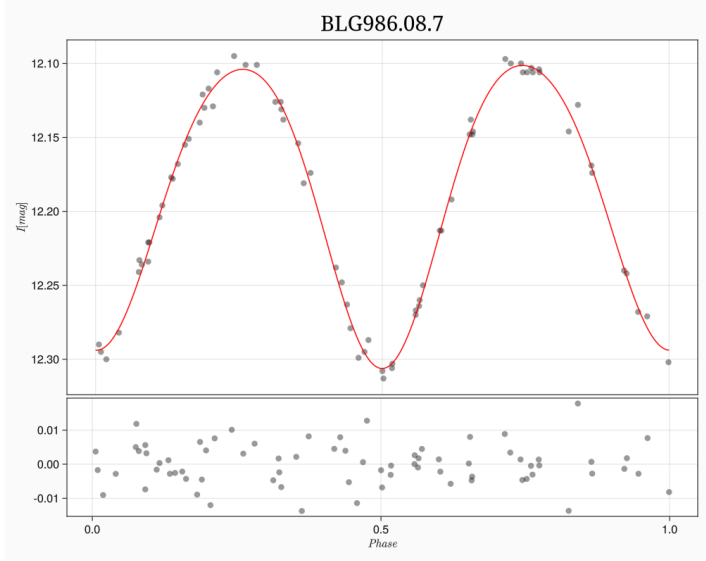
Appendices

Appendix A

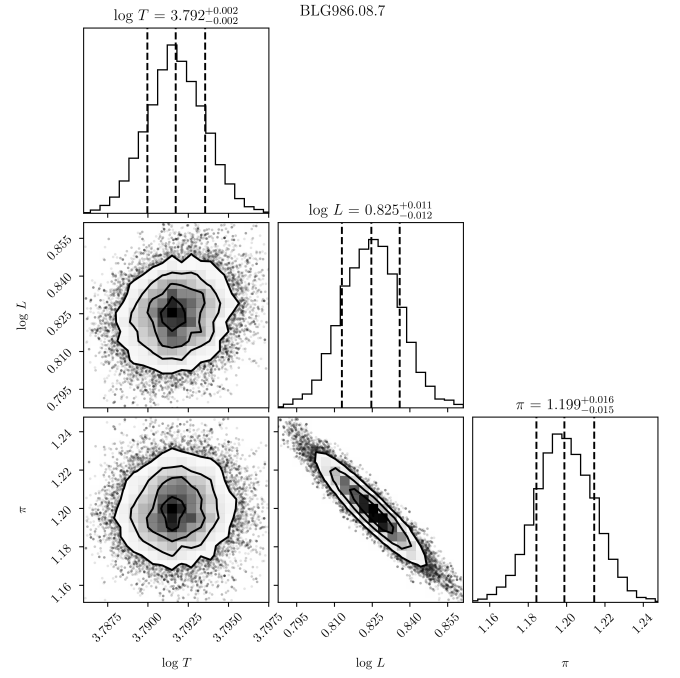
Light curve & SED plots

In the following chapter, spectral energy distribution plots, PARSEC evolutionary tracks, MCMC convergence plots, and phased light curves are presented. For each object, either nearest evolutionary track is plotted, or, in the case of objects that could not be well fitted, some nearest evolutionary tracks are plotted for comparison.

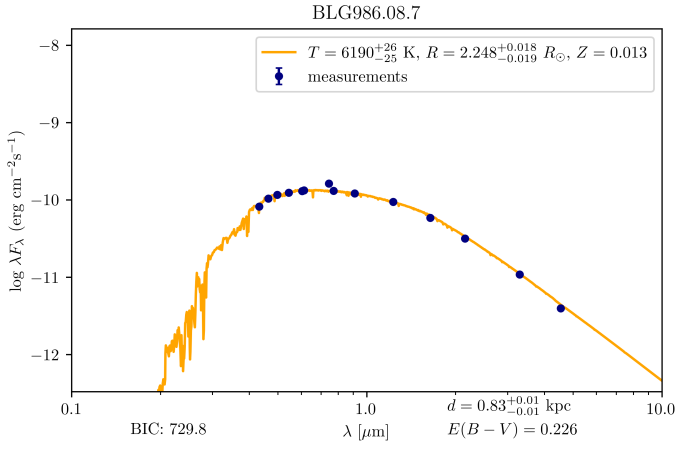
BLG986.08.7



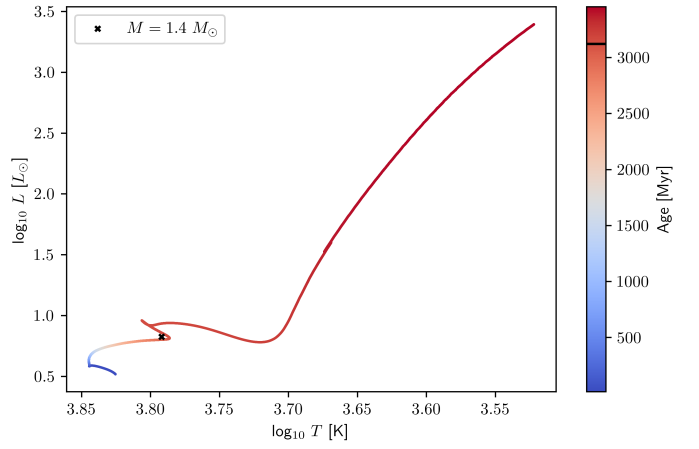
(a) The phased light curve in the I band using OGLE data.



(b) Corner plot for the posterior estimate of SED.

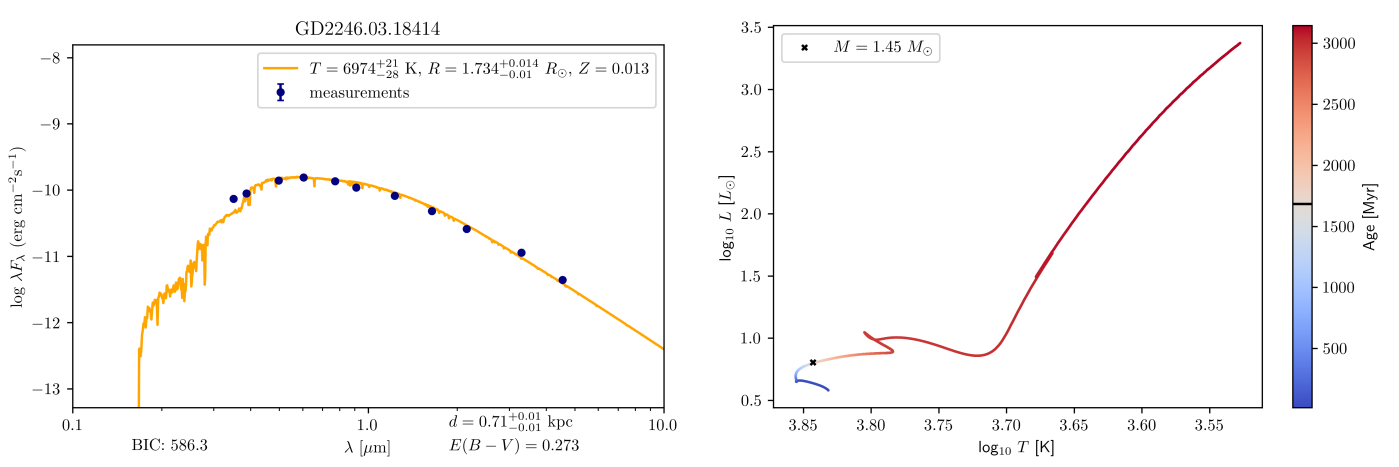
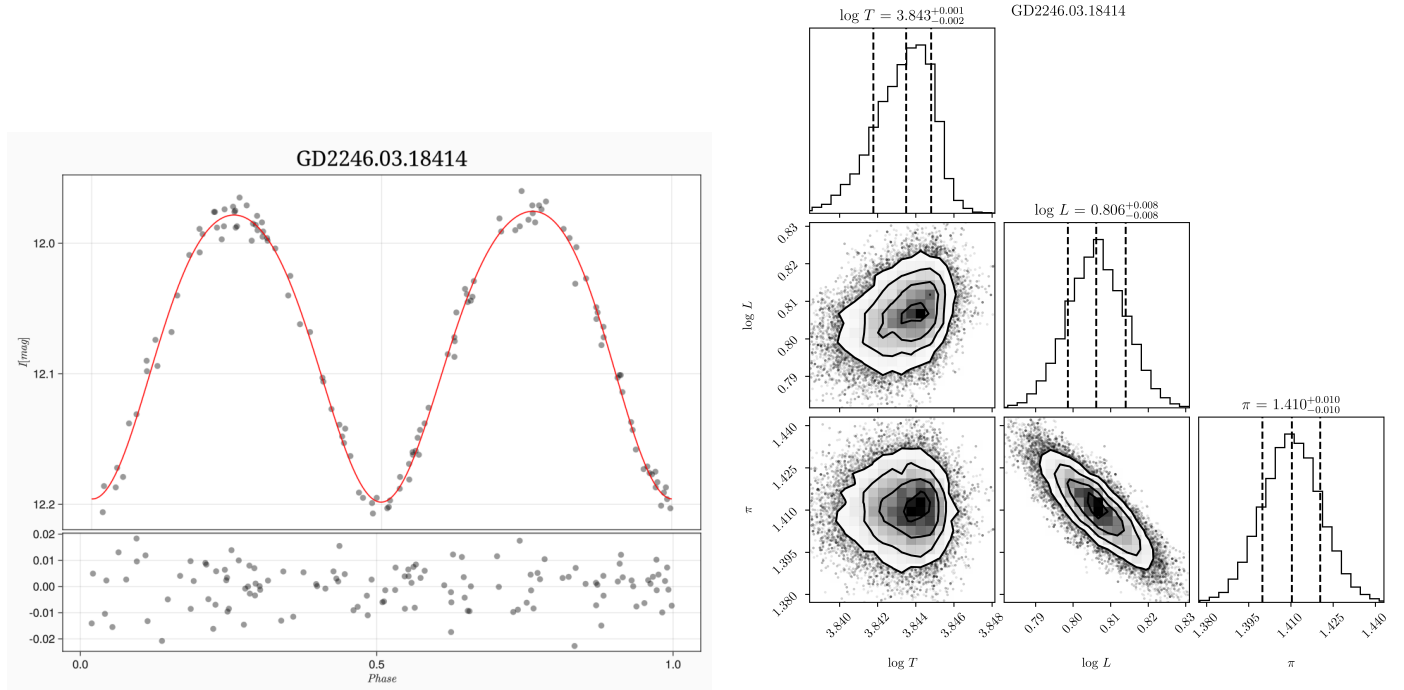


(a) The spectral energy distribution plot for the single star model.

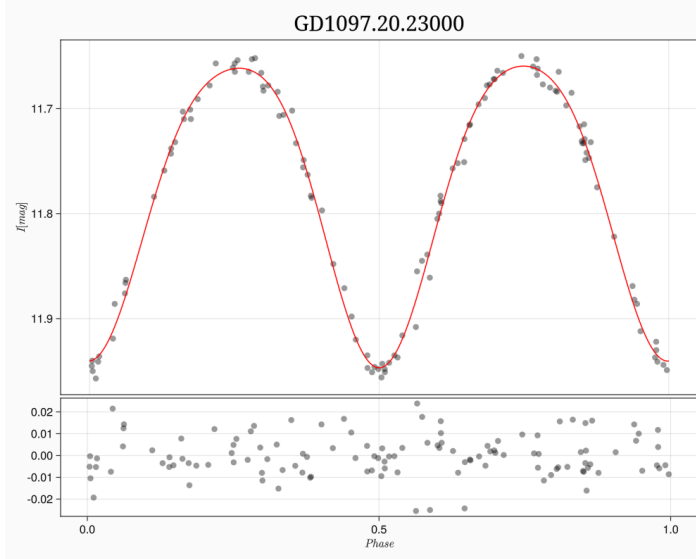


(b) Position in the HR diagram together with the best-fitting PARSEC evolutionary track.

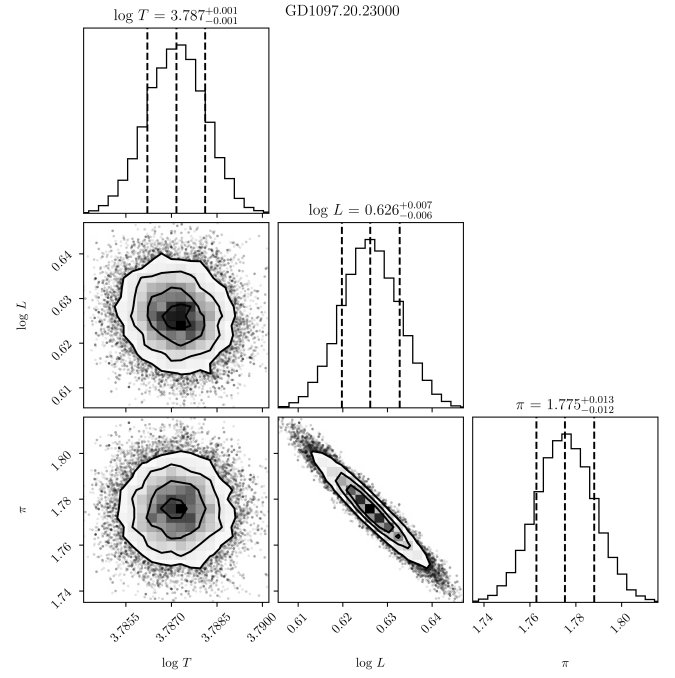
GD2246.03.18414



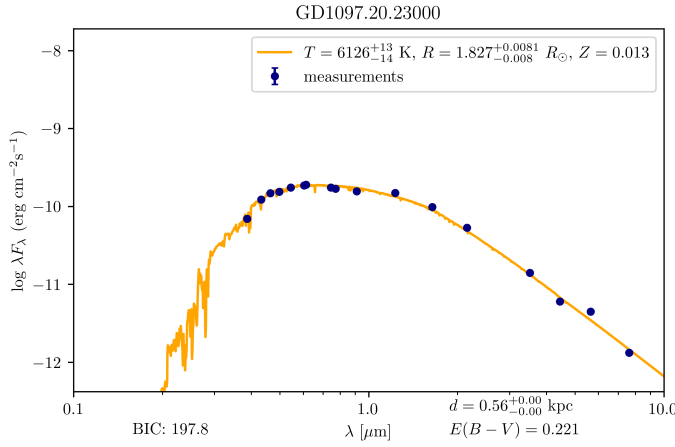
GD1097.20.23000



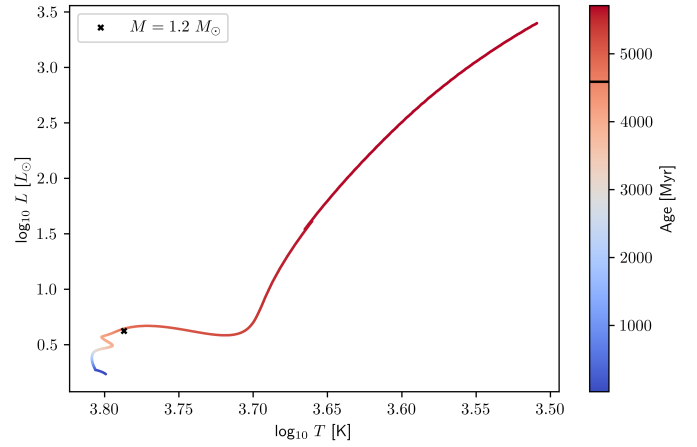
(a) The phased light curve in the I band using OGLE data.



(b) Corner plot for the posterior estimate of SED.

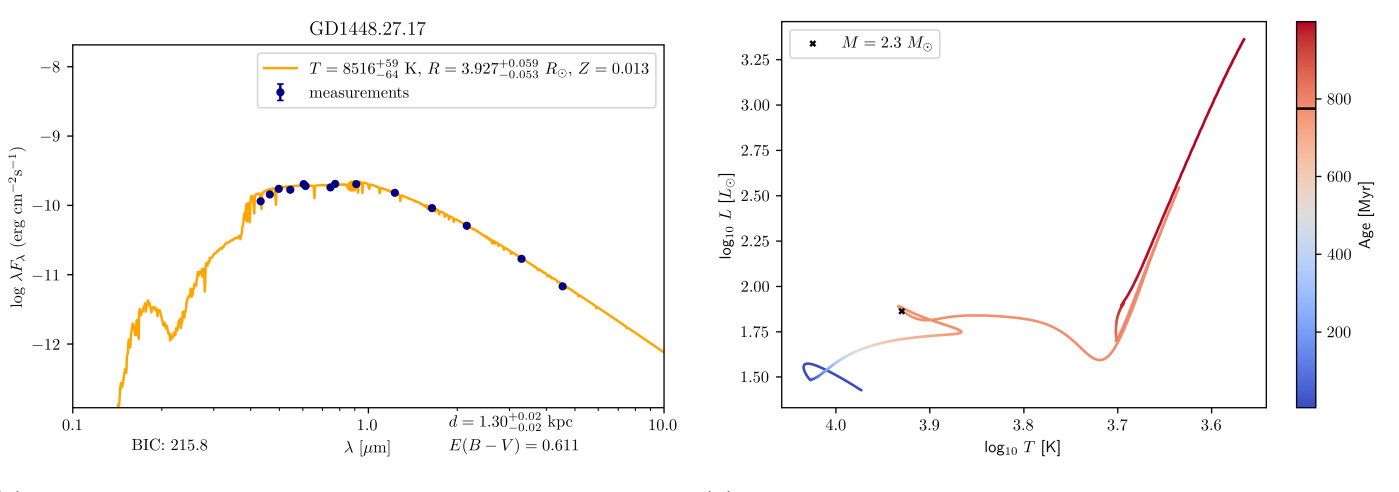
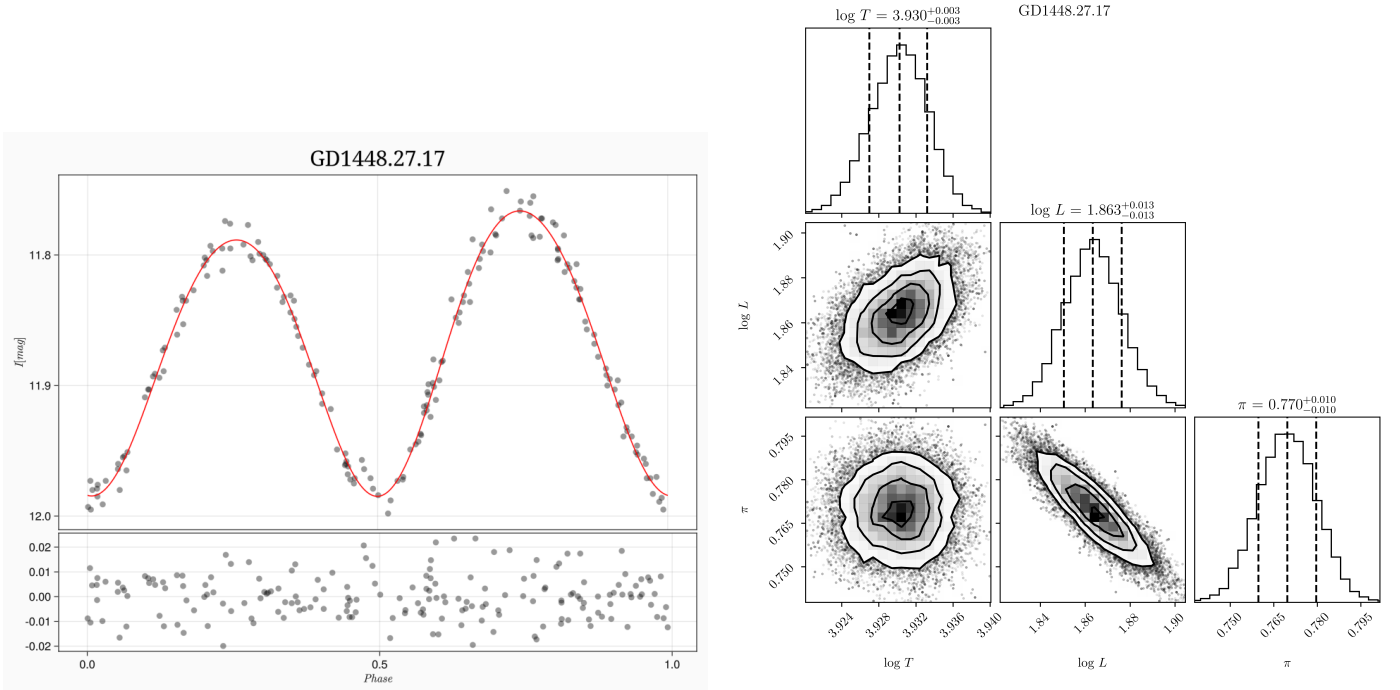


(a) The spectral energy distribution plot for the single star model.

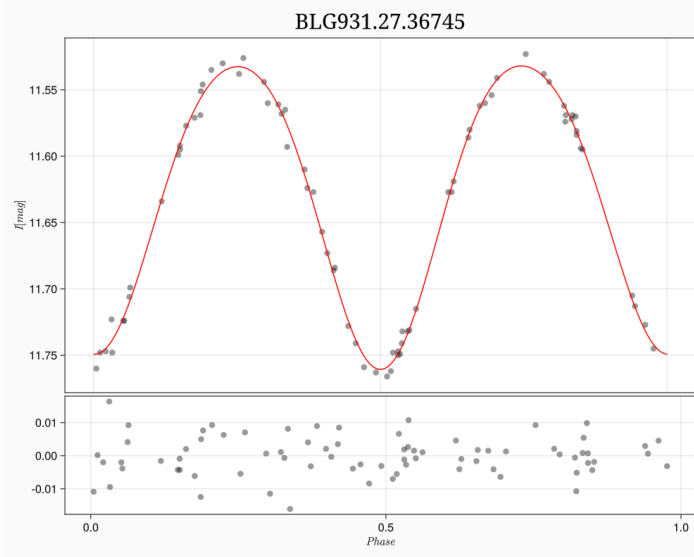


(b) Position in the HR diagram together with the best-fitting PARSEC evolutionary track.

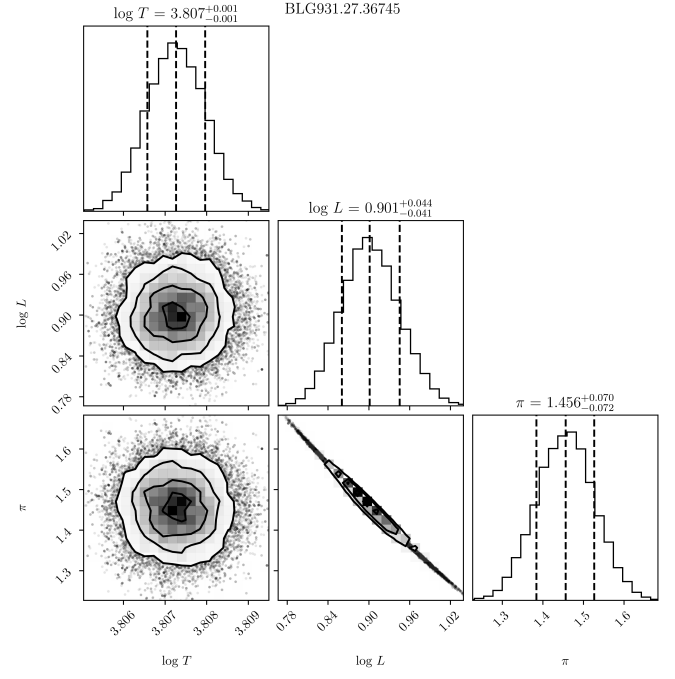
GD1448.27.17



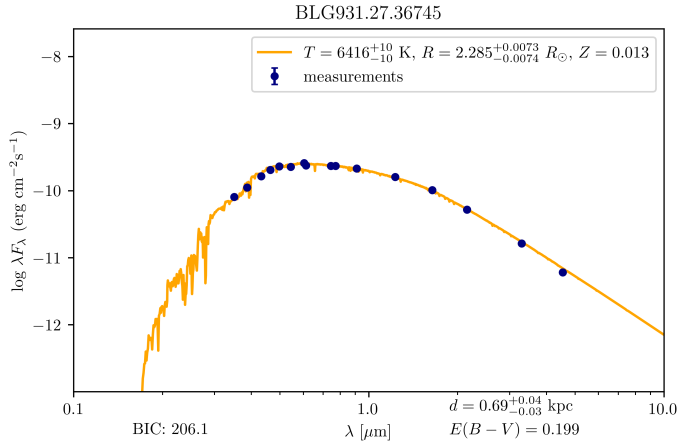
BLG931.27.36745



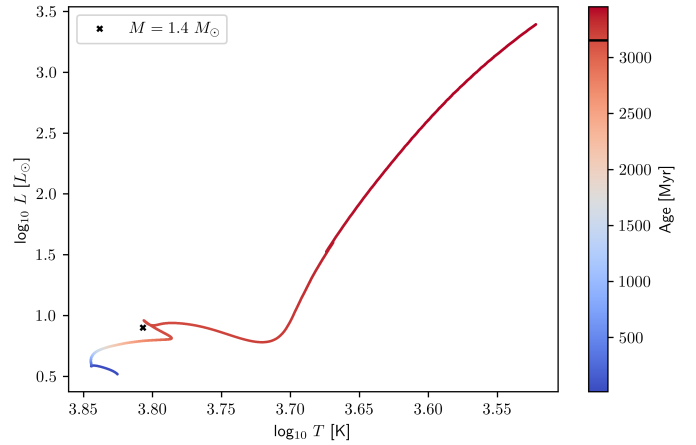
(a) The phased light curve in the I band using OGLE data.



(b) Corner plot for the posterior estimate of SED.

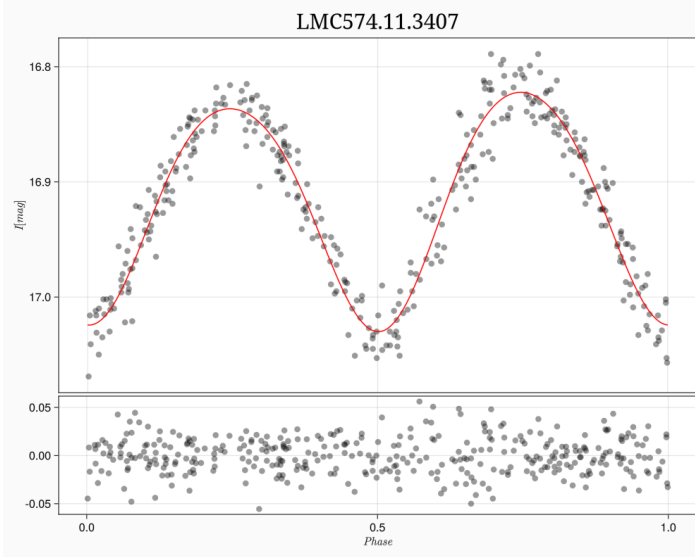


(a) The spectral energy distribution plot for the single star model.

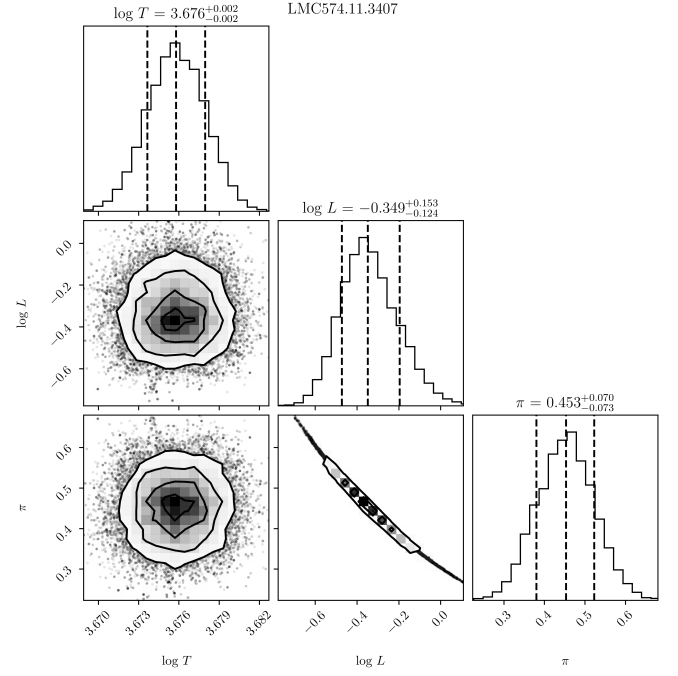


(b) Position in the HR diagram together with the best-fitting PARSEC evolutionary track.

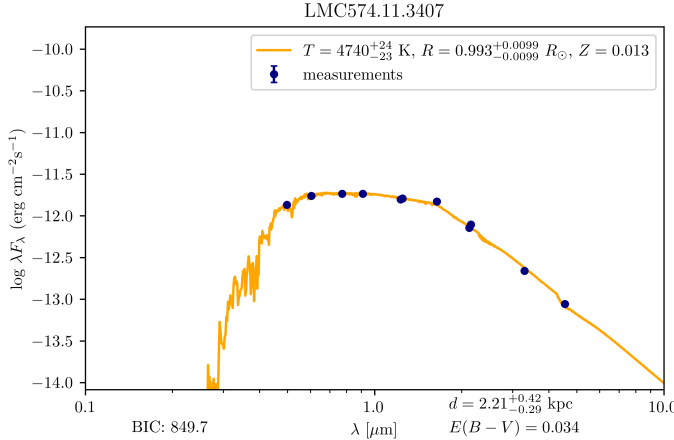
LMC574.11.3407



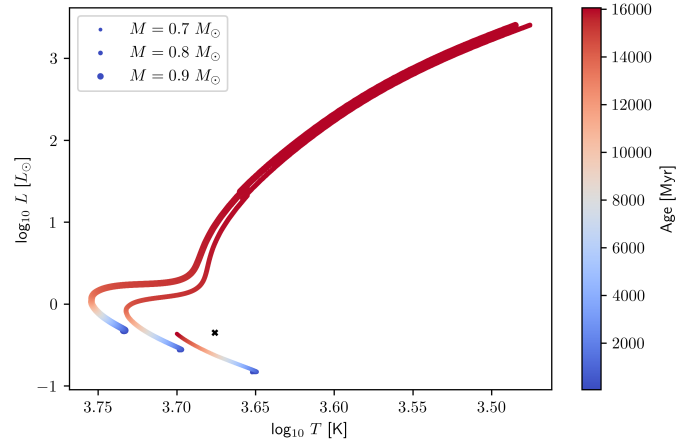
(a) The phased light curve in the I band using OGLE data.



(b) Corner plot for the posterior estimate of SED.

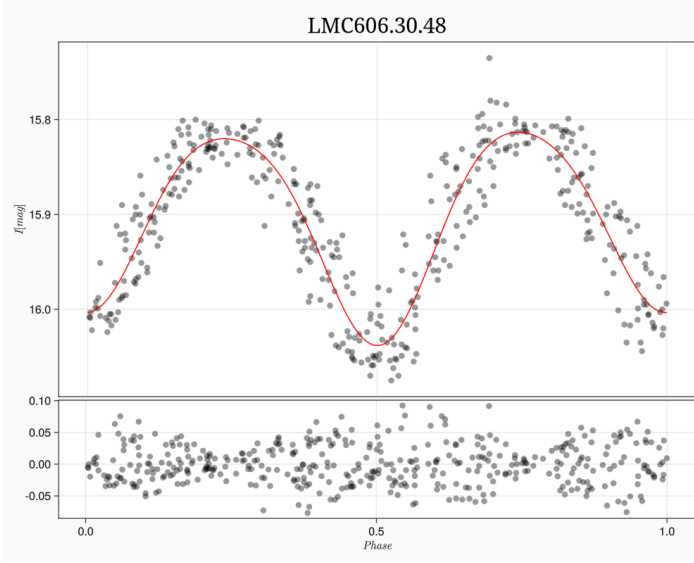


(a) The spectral energy distribution plot for the single star model.

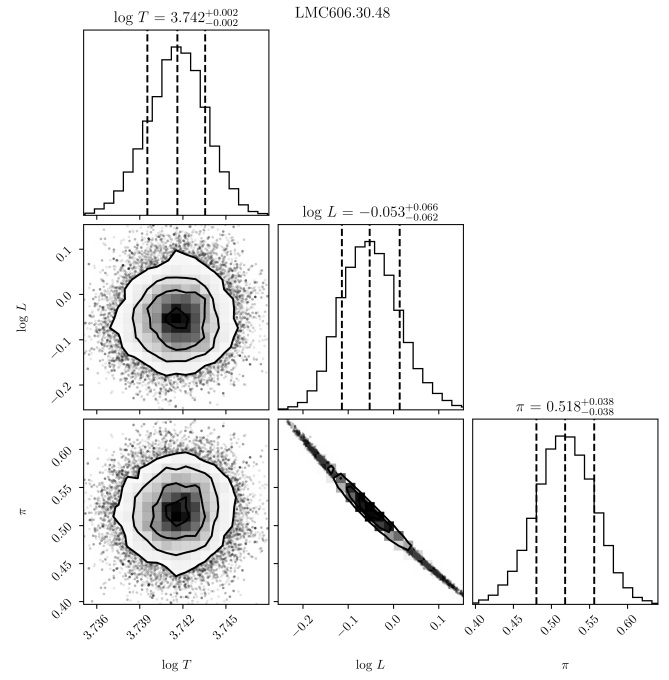


(b) Position in the HR diagram together with the best-fitting PARSEC evolutionary track.

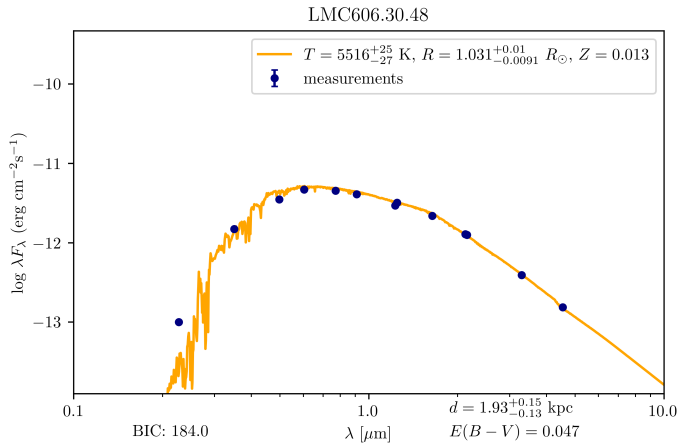
LMC606.30.48



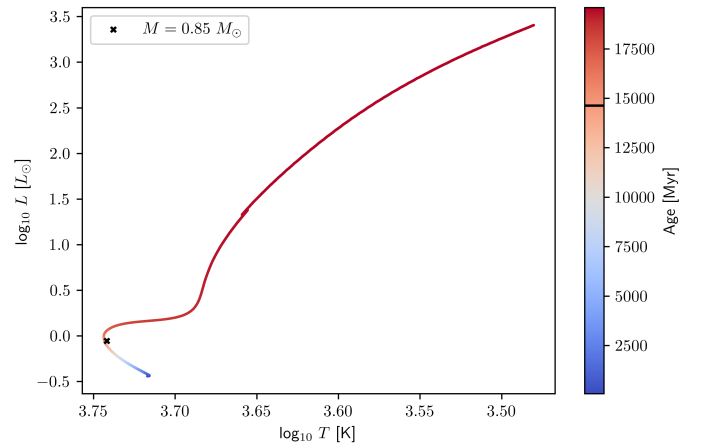
(a) The phased light curve in the I band using OGLE data.



(b) Corner plot for the posterior estimate of SED.

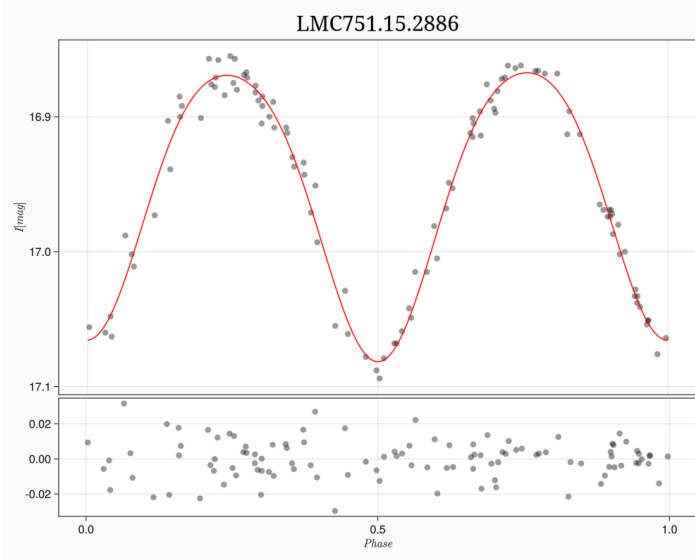


(a) The spectral energy distribution plot for the single star model.

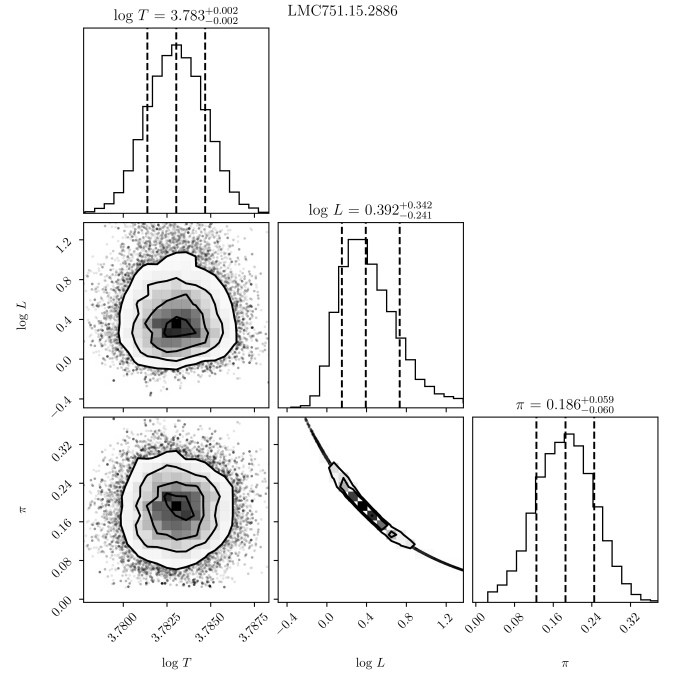


(b) Position in the HR diagram together with the best-fitting PARSEC evolutionary track.

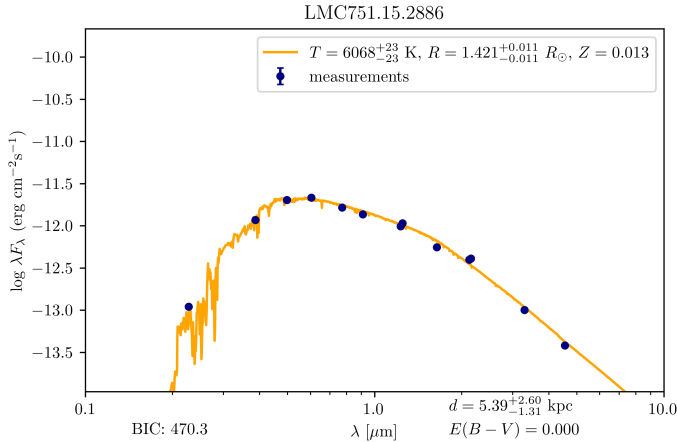
LMC751.15.2886



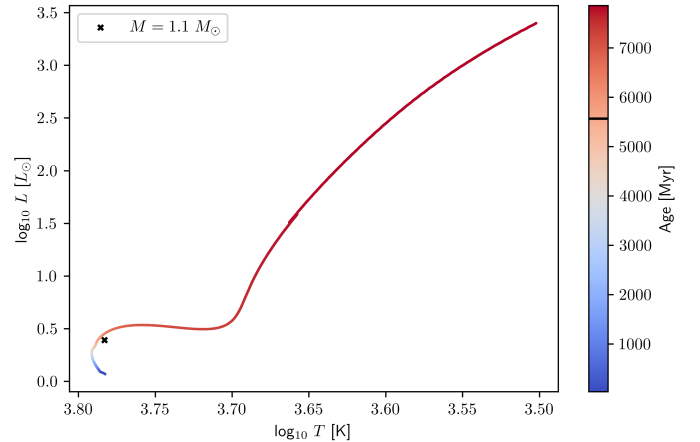
(a) The phased light curve in the I band using OGLE data.



(b) Corner plot for the posterior estimate of SED.

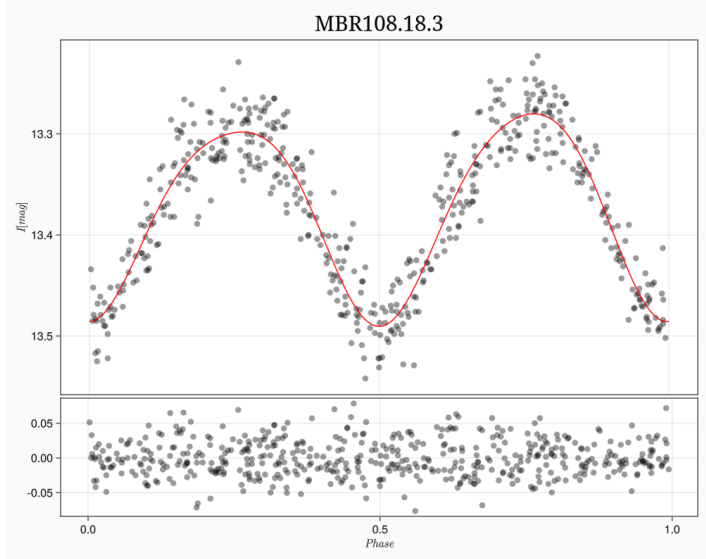


(a) The spectral energy distribution plot for the single star model.

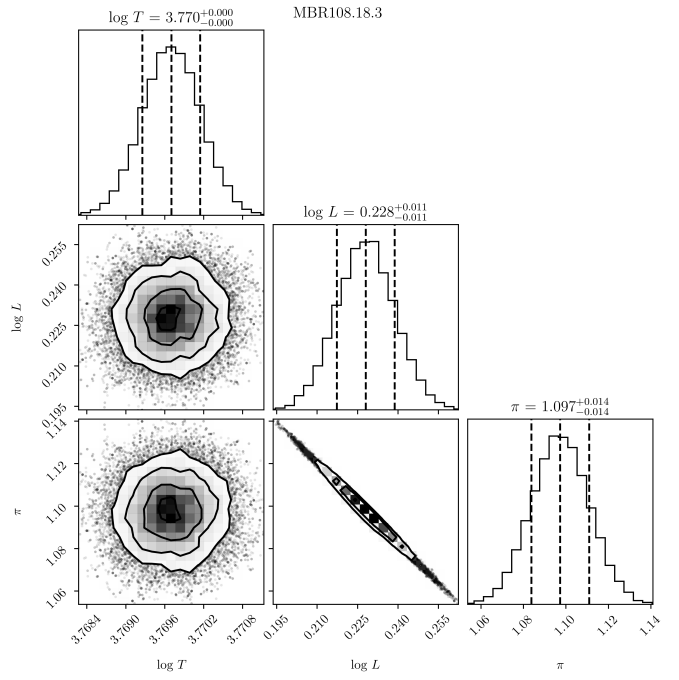


(b) Position in the HR diagram together with the best-fitting PARSEC evolutionary track.

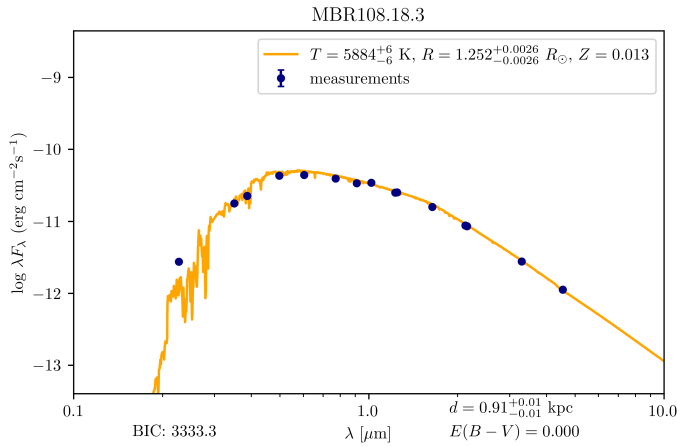
MBR108.18.3



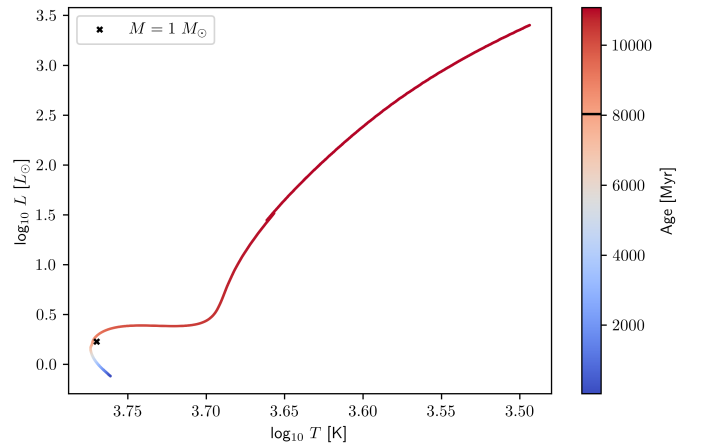
(a) The phased light curve in the I band using OGLE data.



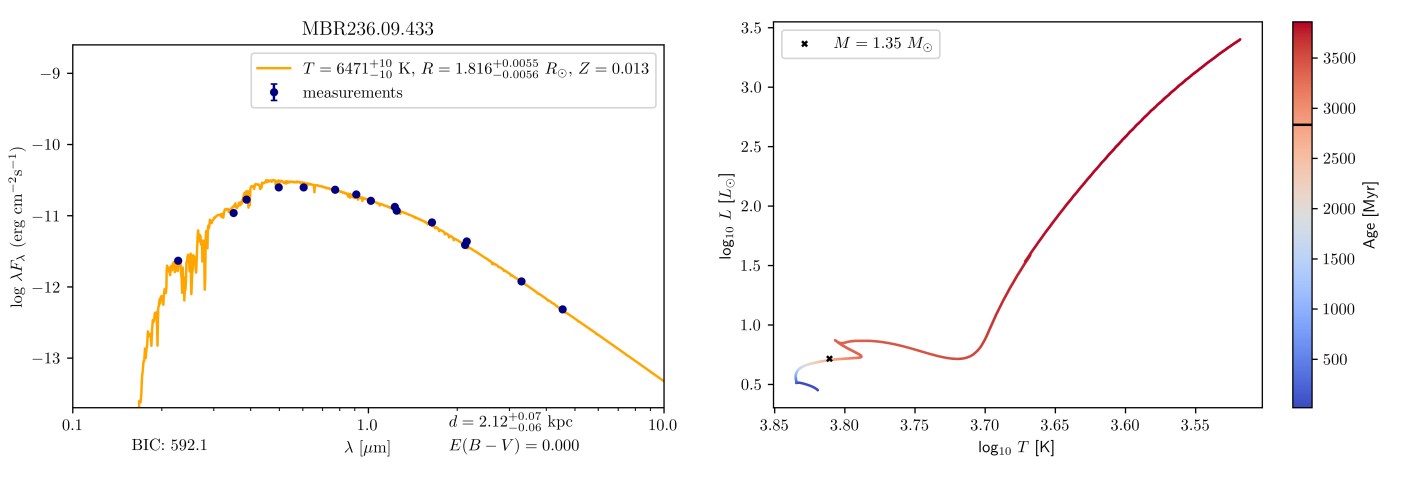
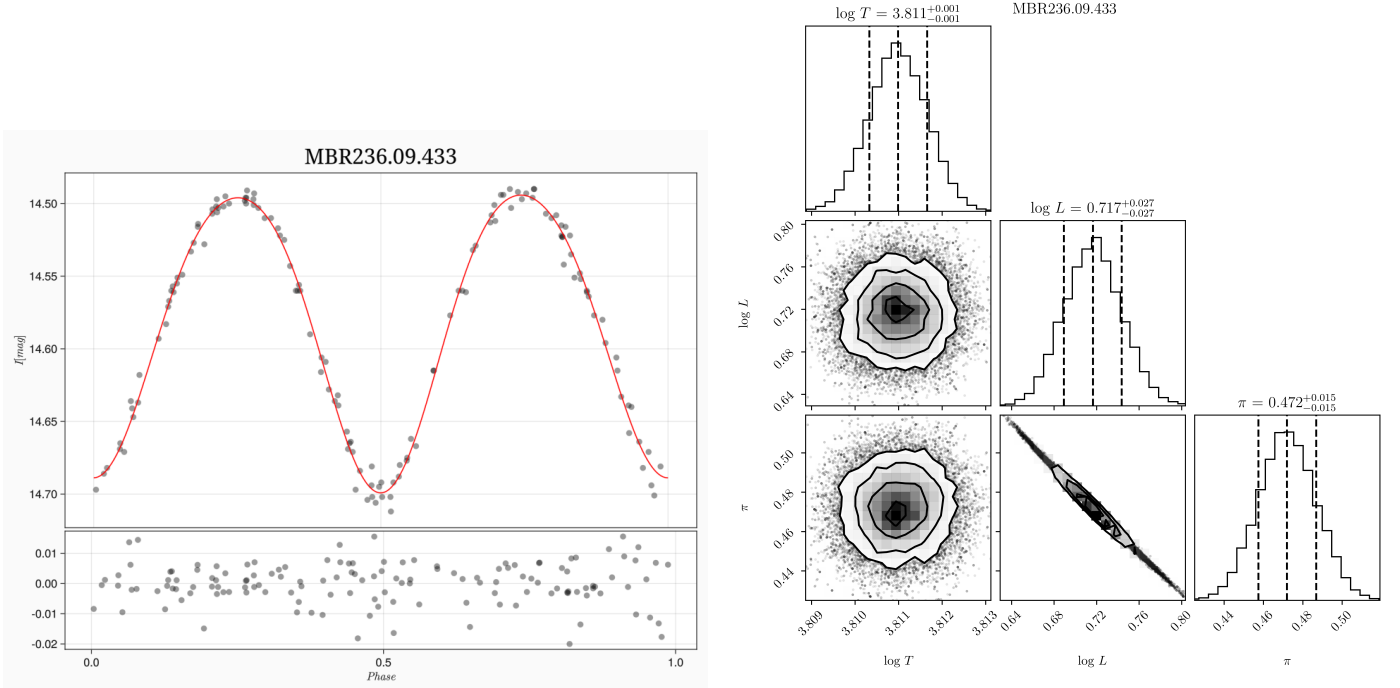
(b) Corner plot for the posterior estimate of SED.



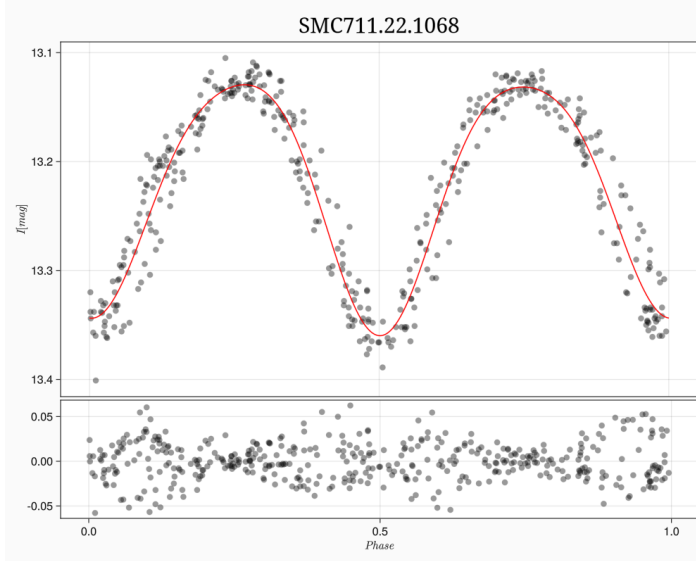
(a) The spectral energy distribution plot for the single star model.



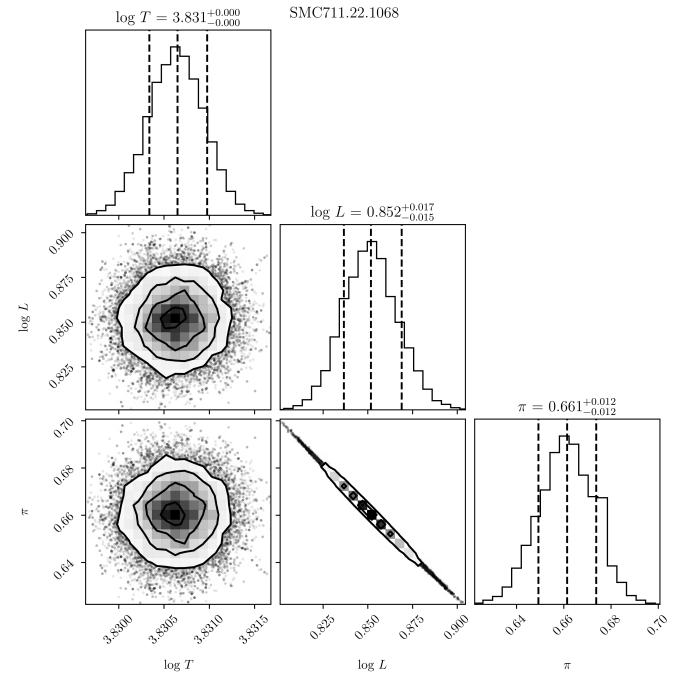
MBR236.09.433



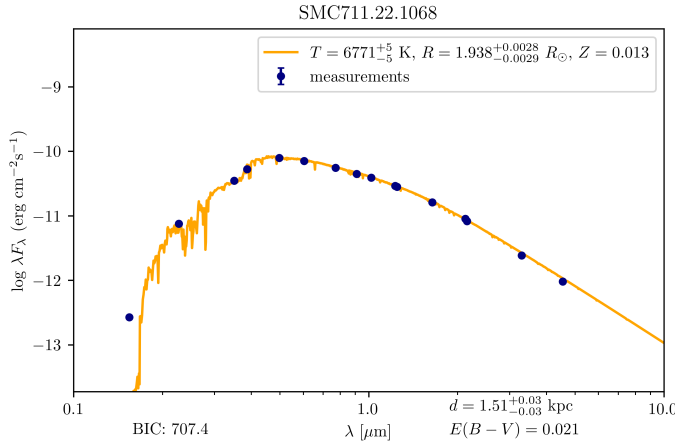
SMC711.22.1068



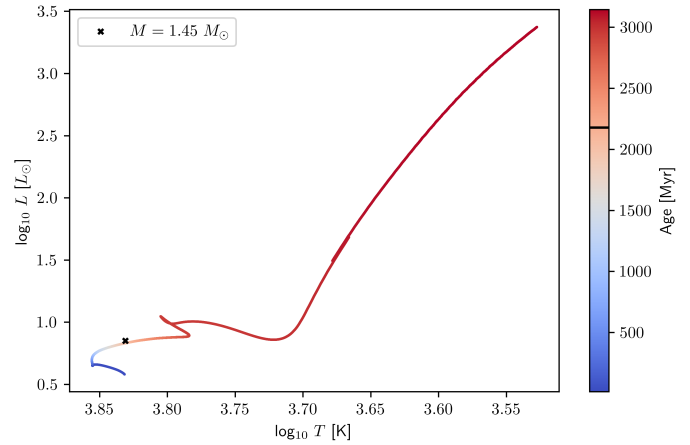
(a) The phased light curve in the I band using OGLE data.



(b) Corner plot for the posterior estimate of SED.

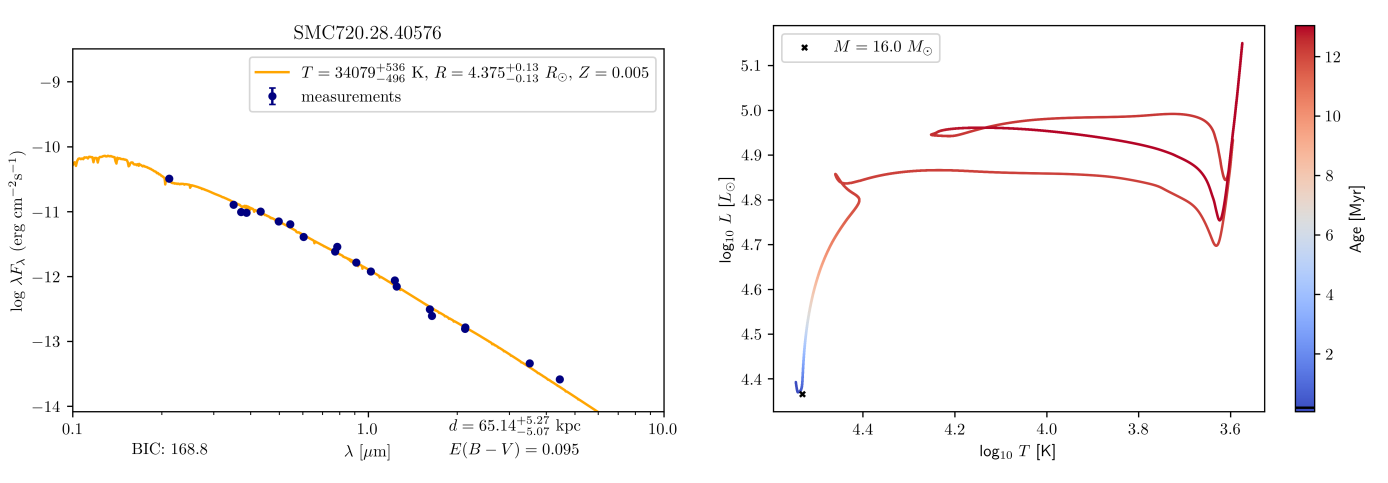
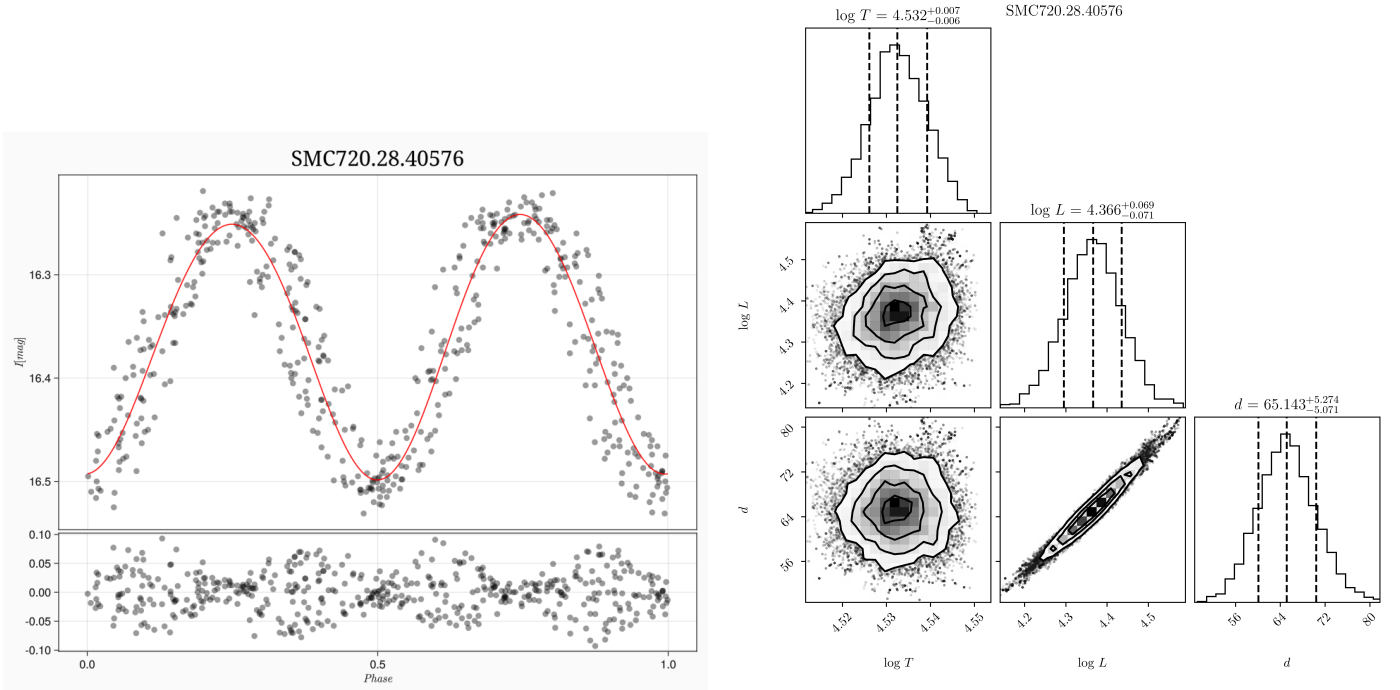


(a) The spectral energy distribution plot for the single star model.

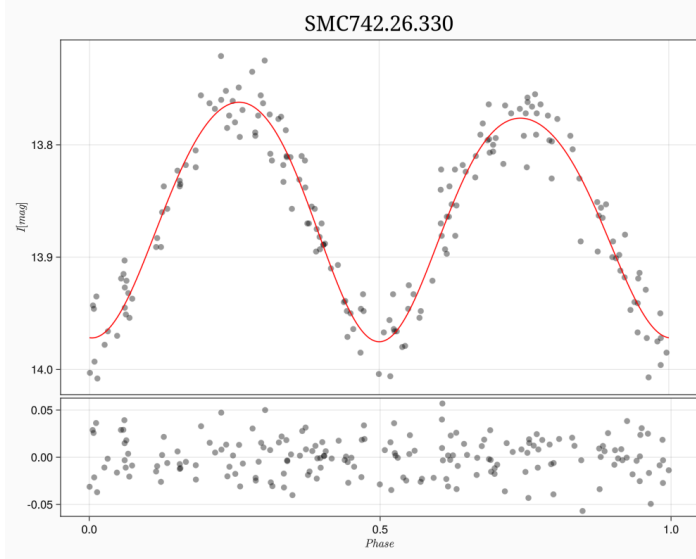


(b) Position in the HR diagram together with the best-fitting PARSEC evolutionary track.

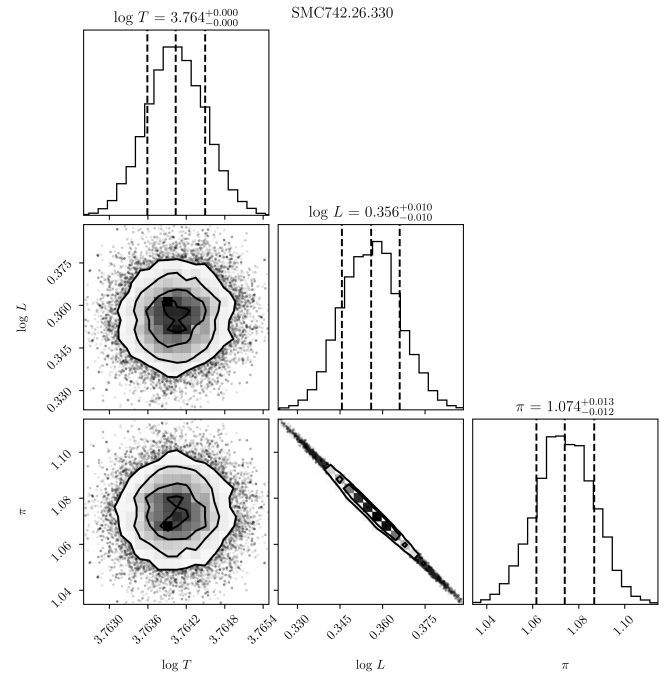
SMC720.28.40576



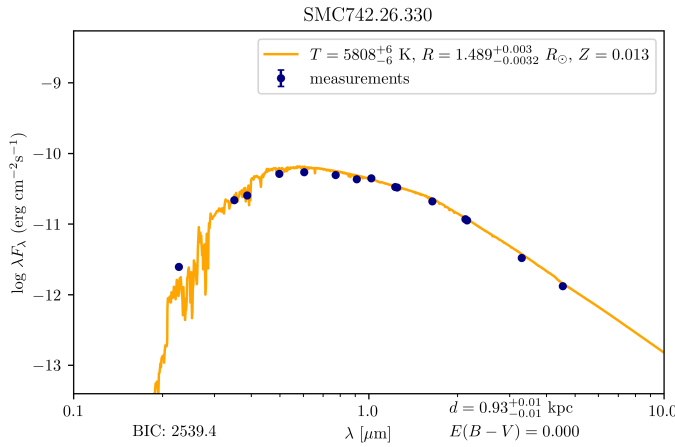
SMC742.26.330



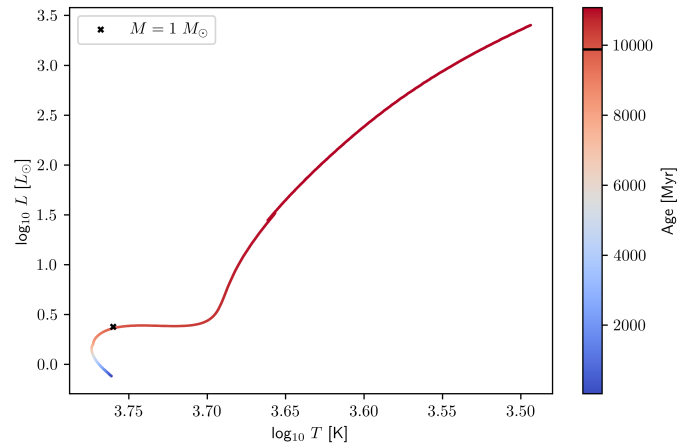
(a) The phased light curve in the I band using OGLE data.



(b) Corner plot for the posterior estimate of SED.



(a) The spectral energy distribution plot for the single star model.



(b) Position in the HR diagram together with the best-fitting PARSEC evolutionary track.

Appendix B

Semiamplitude estimate from Gaia DR3

Let us now assume that a radial velocity can be factored into two separate movements: the centre of mass movement (with velocity v_0) and the circular motion with semiamplitude K . Under the following assumptions, one can find that samples of radial velocity can be written as

$$V_i = v_0 + K \cos(2\pi X_i) \quad (\text{B.1})$$

where X_i denote a sample from $\mathcal{U}(0, 1)$. Now one can calculate the variance of this variable using $\text{Var}(x) = \mathbb{E}X^2 - (\mathbb{E}X)^2$.

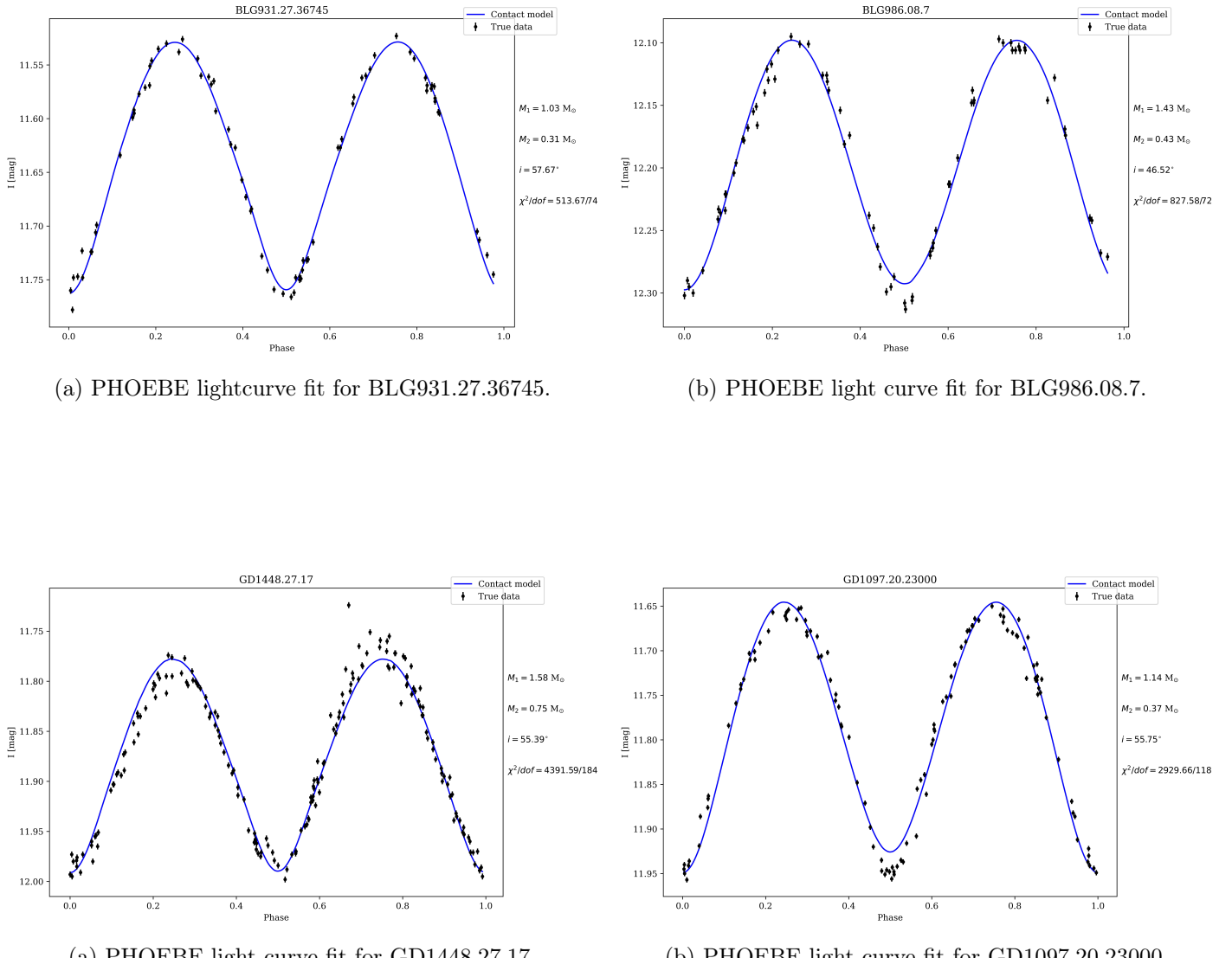
$$\begin{aligned} \mathbb{E}V &= V_0 + \mathbb{E}K \cos(2\pi X) = V_0 \\ \mathbb{E}V^2 &= \mathbb{E}(V_0^2 + \frac{K^2}{2}(1 - \cos(4\pi X)) + 2V_0K \cos(2\pi X)) \\ &= V_0^2 + \frac{K^2}{2} \end{aligned} \quad (\text{B.2})$$

where we used, that expected value of the sinusoidal signal is zero. Hence

$$\text{Var}(V) = \frac{K^2}{2} + V_0^2 - V_0^2 = \frac{K^2}{2}. \quad (\text{B.3})$$

Appendix C

Light curve modelling



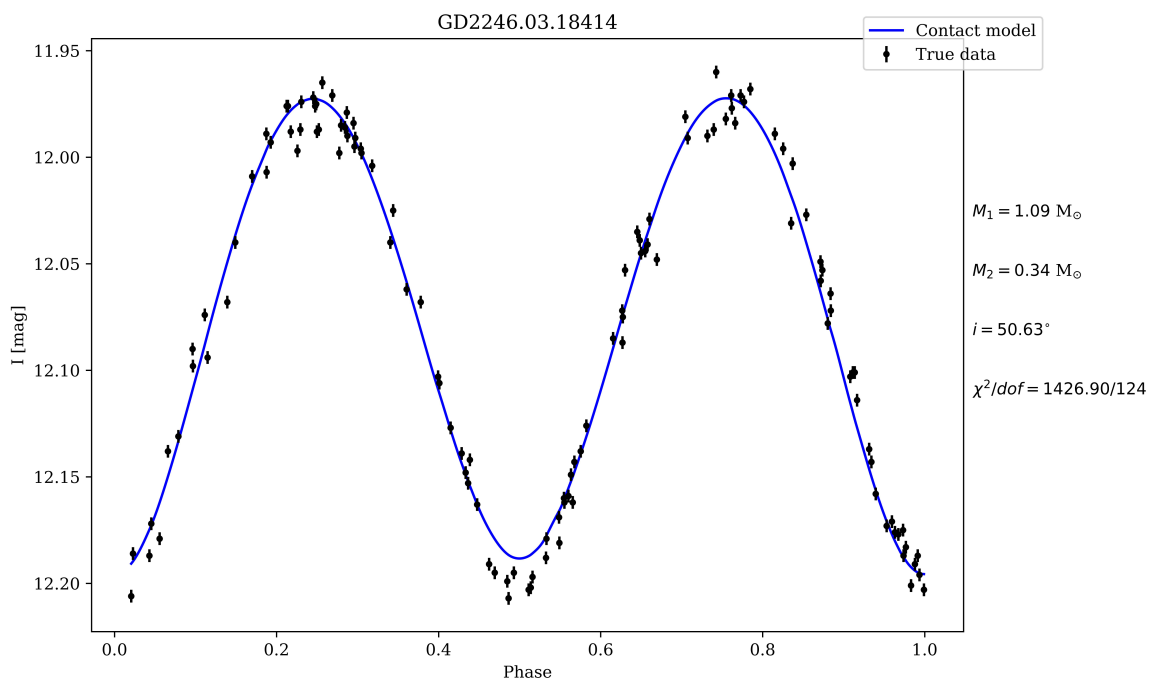


Figure C.3: PHOEBE light curve fit for GD2246.03.18414.